

Drop impact on viscous liquid films

Vatsal Sanjay¹ †‡, Srinath Lakshman¹ †¶, Pierre Chantelot¹ †||, Jacco H. Snoeijer¹ ††, and Detlef Lohse^{1,2} ‡‡

¹Physics of Fluids Group, Max Planck Center for Complex Fluid Dynamics, Department of Science and Technology, MESA+ Institute for Nanotechnology, and J. M. Burgers Centre for Fluid Dynamics, University of Twente, P. O. Box 217, 7500 AE Enschede, The Netherlands

²Max Planck Institute for Dynamics and Self-Organization, Am Fassberg 17, 37077 Göttingen, Germany

(Received xx; revised xx; accepted xx)

When a liquid drop falls on a solid substrate, the air layer in between them delays the occurrence of liquid–solid contact. For impacts on smooth substrates, the air film can even prevent wetting, allowing the drop to bounce off with dynamics identical to that observed for impacts on superamphiphobic materials. In this article, we investigate similar bouncing phenomena, occurring on viscous liquid films, that mimic atomically smooth substrates, with the goal to probe their effective repellency. We elucidate the mechanisms associated to the bouncing to non-bouncing (floating) transition using experiments, simulations, and a minimal model that predicts the main characteristics of drop impact, the contact time, and the coefficient of restitution. In the case of highly viscous or very thin films, the impact dynamics are not affected by the presence of the viscous film. Within this substrate-independent limit, bouncing is suppressed once the drop viscosity exceeds a critical value as on superamphiphobic substrates. For thicker or less viscous films, both the drop and film properties influence the rebound dynamics and conspire to inhibit bouncing above a critical film thickness. This substrate-dependent regime also admits a limit, for low viscosity drops, in which the film properties alone determine the limits of repellency.

Key words:

1. Introduction

Liquid drop impact on solids and liquids abound in nature (Yarin *et al.* 2017) and are essential for several industrial applications, such as inkjet printing (Lohse 2022) and criminal forensics (Smith *et al.* 2018). Consequently, drop impact has garnered extensive attention (Rein 1993; Weiss & Yarin 1999; Thoroddsen *et al.* 2008; Yarin 2006; Josserand & Thoroddsen 2016) ever since the seminal work of Worthington (1877, 1908). Impacts can result in either contact or levitation outcomes, depending on whether the air layer trapped between the drop and the substrate drains completely during impact.

For low impact velocities, the buildup of the lubrication pressure in the draining air

† Contributed equally to this work.

‡ Email address for correspondence: vatsalsanjay@gmail.com

¶ Email address for correspondence: s.lakshman@utwente.nl

|| Email address for correspondence: p.r.a.chantelot@utwente.nl

†† Email address for correspondence: j.h.snoeijer@utwente.nl

‡‡ Email address for correspondence: d.lohse@utwente.nl

layer prevents the drop from contacting with the underlying surface, leading to drop bouncing/floating on this layer (Reynolds 1881; Davis *et al.* 1989; Yiantzios & Davis 1990, 1991; Smith *et al.* 2003; van der Veen *et al.* 2012). Drops that bounce/float in such a scenario are realized in several configurations, for example on solid surfaces (Kolinski *et al.* 2014; de Ruiter *et al.* 2015), liquid films (Pan & Law 2007; Hao *et al.* 2015; Tang *et al.* 2018, 2019), stationary (Rodriguez & Mesler 1985; Klyuzhin *et al.* 2010; Wu *et al.* 2020) or vibrating liquid pools (Couder *et al.* 2005*a,b*), or even soap films (Gilet & Bush 2009). Interfacial processes such as Marangoni flow (Geri *et al.* 2017) or the generation of vapor below a drop deposited on a superheated substrate (the Leidenfrost effect where the liquid levitates on a cushion of its own vapor, Leidenfrost 1756; Quéré 2013; Chantelot & Lohse 2021) can further stabilize the sandwiched air/vapor layer to facilitate levitation, even for the dynamic case of drop impact (Chandra & Avedisian 1991; Tran *et al.* 2012; Shiota *et al.* 2016). Drops can also defy gravity and levitate thanks to the so-called inverse Leidenfrost effect (Adda-Bedia *et al.* 2016; Gauthier *et al.* 2019), or electromagnetic forces (Pal *et al.* 2017; Singh *et al.* 2018).

At higher impact velocities, the air layer ruptures, leading to contact. The rupture occurs due to a strong van der Waals attractive force between the droplet and the solid or liquid substrate, which comes into play as the thickness of the air layer reduces below the order of 10 – 100 nm (see appendix A, and Charles & Mason 1960; Chubynsky *et al.* 2020; Zhang *et al.* 2021*b*). Additionally, surface asperities that are of the order of the minimum gas layer thickness can also cause rupture, binding the drop to the surface (Thoroddsen *et al.* 2003; Kolinski *et al.* 2014; Li *et al.* 2015).

In this work, we focus on levitation outcomes which can be classified as either repellent (bouncing drops) or non-bouncing (non-repellent/floating) behaviors. We note that non-repellent scenarios ultimately lead to coalescence, a phenomenon we do not investigate here and that occurs on a time scale much larger than that of impact (Lo *et al.* 2017; Duchemin & Josserand 2020). We perform experiments and direct numerical simulations (DNS) to investigate drop rebound on viscous liquid films. In the limit of thin enough viscous coatings, the substrate mimics an atomically smooth solid and displays a superamphiphobic-like repellent behavior (Hao *et al.* 2015; Lo *et al.* 2017). This substrate-independent bouncing (Gilet & Bush 2012; Pack *et al.* 2017; Lakshman *et al.* 2021) can be compared with that observed on superhydrophobic substrates, where the apparent contact time is given by the oscillation time of a drop (Rayleigh 1879), owing to the drop impact-oscillation analogy (Richard *et al.* 2002). As a result, such an impacting drop can be modeled using a quasi-ideal spring, whose stiffness is given by the surface tension coefficient (Okumura *et al.* 2003). Unlike ideal Rayleigh oscillations, the collisions are partially inelastic due to viscous dissipation (Prosperetti 1977). When the drop viscosity increases and viscous dissipation becomes significant, this spring couples with a linear damper whose strength is proportional to the drop's viscosity (see appendix B, and Jha *et al.* 2020). The adoption of such a spring-mass-damper system has led to several successful predictions of the drop impact dynamics in a variety of configurations such as viscous bouncing (Moláček & Bush 2012; Jha *et al.* 2020), spontaneous levitation (Schutzius *et al.* 2015), fast bouncing (Chantelot *et al.* 2018), and walking drops (Terwagne *et al.* 2013).

In the opposing limit of thick liquid films (pools), drops can also bounce/float (Reynolds 1881; Jayaratne & Mason 1964). However, unlike solids and very thin films, these pools deform on impact and can absorb a part of the impact kinetic energy in the form of (i) surface energy owing to interfacial deformation, (ii) internal kinetic energy, and (iii) viscous dissipation (Galeano-Rios *et al.* 2021). Consequently, the impact outcomes also include a substrate-dependent regime which culminates in the transition

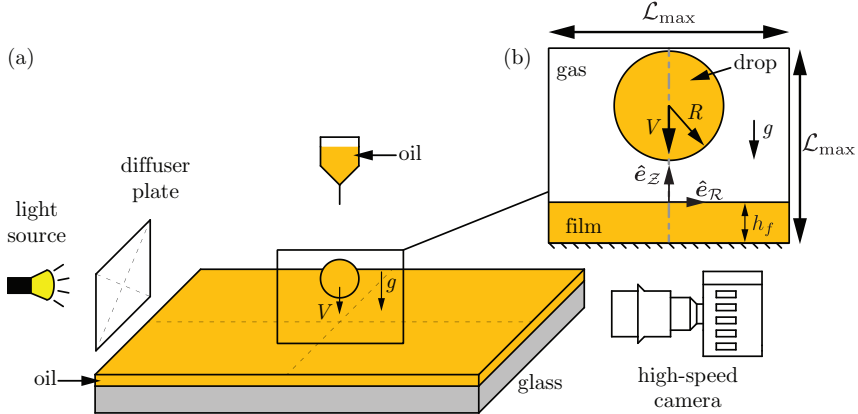


FIGURE 1. (a) Schematic (not to scale) of the experimental setup. (b) Side view visualization of the drop impact process as viewed using the high-speed camera. The inset also shows the axi-symmetric domain used in the direct numerical simulations and defines the used symbols. The domain boundaries are chosen to be far enough not to influence the drop impact process. Furthermore, we ensure that the waves formed on the film are not reflected back from these boundaries. Consequently, for $Oh_f < 0.1$, $L_{\max} \gg 8R$. On the other hand, $Oh_f > 0.1$ and waves on the film are damped, we choose $L_{\max} = 8R$.

from bouncing to non-bouncing (floating). In the latter case, the drop cannot take off, resulting in the liquid surface loosing its repellent property. [Hao et al. \(2015\)](#) studied this transition from the substrate-independent to substrate-dependent bouncing for water drops, and reported that the critical film thickness marking this transition depends on the film viscosity and the impact velocity of the drops.

In the present work, we elucidate how the thickness and viscosity of liquid coatings influence the rebound characteristics of an impacting drop, culminating in the loss of repellency: the transition from bouncing to non-bouncing (floating). We disentangle how the initial kinetic energy of an impacting drop can be absorbed through dissipation and energy transfers in the drop and the liquid film.

The paper is organized as follows: § 2 describes the experimental and numerical methods. In § 3, we discuss the phenomenology of the drop impact dynamics on viscous liquid films. Guided by our experimental and numerical observations, we develop a phenomenological model in § 4, extending on the spring-mass-damper analogy by considering the liquid coating as an additional source of dissipation. In § 5, we test the validity and applicability of this model by comparing the predicted values of the coefficient of restitution with our observations when both the drop and film properties are varied. We also delineate the various regimes observed in this work by measuring the critical film thicknesses at which the substrate-independent to substrate-dependent and bouncing to non-bouncing (floating) transitions occur and compare their observed values with the model predictions. Further, § 6 investigates the cases where our phenomenological model fails to predict the observed dynamics and gives alternate explanations. The paper ends with a conclusions and an outlook (§ 7).

2. Methods

2.1. Experimental details

Our experiments, whose setup is sketched in figure 1, consist of silicone oil droplets with radius R , density ρ_d , and viscosity η_d , impacting on silicone oil films with thickness

Silicone oil	ρ (kg/m ³)	η (mPa.s)	γ (mN/m)
SE 1	818	0.8	17
AK 5	920	4.6	19
AK 10	930	9.3	20
AK 20	950	19	21
AK 35	960	34	21
AK 50	960	48	21
AK 100	960	96	21

TABLE 1. Properties of the liquids used in the experiments. ρ and η are the density of the liquids and γ denotes the liquid-air surface tension coefficient. Throughout the manuscript, the subscripts d , f , and s represent drop, film, and surrounding, respectively. The silicone oil manufacturers are Shin Etsu (SE) and Wacker Chemie AG (AK).

*h*_f, density ρ_f , and viscosity η_f . We choose silicone oil as a working fluid as its viscosity can be varied over a wide range, here from 0.8 mPa.s to 96 mPa.s, while keeping its density and surface tension coefficient γ nearly constant, as evidenced in table 1. Droplets with radius $R = 1.0 \pm 0.1$ mm are released from a calibrated needle whose height can be varied to adjust the impact velocity V from 0.1 m/s to 0.5 m/s. The rupture of the air layer, that mediates the interaction between the drop and the film, determines the upper bound of the bouncing regime. This rupture sets the critical impact velocity, expressed as the Weber number (*i.e.*, the ratio of inertial to capillary stresses) $We_d \equiv \rho_d R V^2 / \gamma \lesssim \mathcal{O}(10)$, above which coalescence between the miscible drop and film occurs (see appendix A and Chubynsky *et al.* 2020; Sharma & Dixit 2021). We further fix the impact velocity at $V = 0.3 \pm 0.03$ m/s, corresponding to $We_d = 4 \pm 1$, and focus on the influence of the material properties of the drop and the film on the impact process (see § 2.2). Indeed, this process is fairly independent of We_d in the narrow range of We_d in which bouncing occurs without air layer rupture (see appendices A and C).

Films of controlled thickness, varying from 0.01 mm to 1 mm, are prepared by spin-coating the liquid for $h_f < 0.03$ mm, or by depositing a known volume of silicone oil on a glass slide and allowing it to spread when $h_f > 0.03$ mm. We measure the thickness of spincoated films using reflectometry (Reizman 1965), with an uncertainty of ± 0.1 μ m, while the thicker films obtained from the deposition method are characterized from side-view imaging, using a procedure detailed in appendix D, with an uncertainty of ± 30 μ m. We record the impact dynamics using high-speed side-view imaging at 10,000 frames per second (Photron UX100).

2.2. Governing equations & Numerical framework

This section describes the direct numerical simulation (DNS) framework used to study the drop impact process with the free software program, *Basilisk C* (Popinet & Collaborators 2013–2022a), using the volume of fluid method (VoF, equation (2.1)) for tracking the interface (Tryggvason *et al.* 2011). In this work, we have three fluids, namely, the drop, film, and air, denoted by (d) , (f) , and (a) , respectively (figure 1). In order to track the three fluids and enforce non-coalescence between the drop and the film, we use two VoF tracer fields, Ψ_1, Ψ_2 (Ramírez-Soto *et al.* 2020),

$$\left(\frac{\partial}{\partial t} + \mathbf{v} \cdot \nabla \right) \{ \Psi_1, \Psi_2 \} = 0, \quad (2.1)$$

where \mathbf{v} is the velocity field. The use of two VoF fields, followed by interface reconstruction and implicit tagging of the ambient medium (air tracer, $\Psi_a = 1 - \Psi_1 - \Psi_2$), ensures that the two tracers never overlap (Ramírez-Soto *et al.* 2020; Naru 2021). As a result, there is always a thin air layer between the drop and the film. Our continuum-based simulations are thus not sufficient to predict the coalescence of interfaces (Chubynsky *et al.* 2020), and we obtain the bounds of the non-coalescence regime, which sets the maximal Weber number probed in our simulations, from experiments (see appendix A for details).

We use adaptive mesh refinement (AMR) to resolve the length scales pertinent to capture the bouncing process, *i.e.* the flow inside the drop and the liquid coating. The adaption is based on minimizing the error estimated using the wavelet algorithm (Popinet 2015) in the volume of fluid tracers, interfacial curvatures, velocity field, vorticity field and rate of viscous dissipation with tolerances of 10^{-3} , 10^{-4} , 10^{-2} , 10^{-2} , and 10^{-3} , respectively (Sanjay 2022). We ensure that at least 15–20 grid cells are present across the minimum liquid film thickness ($\Gamma = h_f/R = 0.01$) studied in this work to resolve the velocity gradients in the film (Josserand *et al.* 2016; Ling *et al.* 2017). The minimum thickness of the air layer is of the order of the minimum grid size $\Delta = R/2048$. We further note that this thickness can be larger than this minimum owing to flow characteristics. For example, the shear stress balance across an interface with a high viscosity ratio delays the drainage of the air layer (Zhang *et al.* 2021a).

For an incompressible flow, the mass conservation requires the velocity field to be divergence-free

$$\nabla \cdot \mathbf{v} = 0. \quad (2.2)$$

Furthermore, the momentum conservation reads (tildes denote dimensionless quantities)

$$\left(\frac{\partial}{\partial \tilde{t}} + \tilde{\mathbf{v}} \cdot \tilde{\nabla} \right) \tilde{\mathbf{v}} = \frac{1}{\tilde{\rho}} \left(-\tilde{\nabla} p + \tilde{\nabla} \cdot (2Oh\tilde{\mathcal{D}}) \right) - Bo \hat{\mathbf{e}}_{\mathbf{z}} + \tilde{\mathbf{f}}_{\gamma}, \quad (2.3)$$

where the coordinate dimensions, velocity field \mathbf{v} , and pressure p are normalized using the drop radius R , inertio-capillary velocity scale $v_{\gamma} = \sqrt{\gamma/\rho_d R}$ and capillary pressure $p_{\gamma} = \gamma/R$, respectively. The bracketed term on the left hand side of equation (2.3) is the material derivative. On the right hand side, $\hat{\mathbf{e}}_{\mathbf{z}}$ is a unit vector in the vertically upward direction (see figure 1b) and the deformation tensor, $\tilde{\mathcal{D}}$ is the symmetric part of the velocity gradient tensor $(\tilde{\mathcal{D}} = (\tilde{\nabla}\tilde{\mathbf{v}} + (\tilde{\nabla}\tilde{\mathbf{v}})^T)/2)$. Further, we employ the one-fluid approximation (Tryggvason *et al.* 2011) to solve these equations whereby the material properties (such as dimensionless density $\tilde{\rho} = \rho/\rho_d$ and dimensionless viscosity Oh) change depending on which fluid is present at a given spatial location (equations (2.4)–(2.5))

$$\tilde{\rho} = \Psi_1 + \Psi_2 \frac{\rho_f}{\rho_d} + (1 - \Psi_1 - \Psi_2) \frac{\rho_a}{\rho_d} \quad (2.4)$$

$$Oh = \Psi_1 Oh_d + \Psi_2 Oh_f + (1 - \Psi_1 - \Psi_2) Oh_a \quad (2.5)$$

where, the Ohnesorge number Oh is the ratio between the inertio-capillary to the visco-capillary time scales. It is defined for all the three phases, namely, the drop, the film, and the air (ambient), and are given by

$$Oh_d = \frac{\eta_d}{\sqrt{\rho_d \gamma R}}, \quad (2.6)$$

$$Oh_f = \frac{\eta_f}{\sqrt{\rho_d \gamma R}}, \text{ and} \quad (2.7)$$

$$Oh_a = \frac{\eta_a}{\sqrt{\rho_d \gamma R}}, \quad (2.8)$$

respectively. Here, η_d , η_f , and η_a are the viscosity of the drop, film and air (ambient), respectively. Furthermore, ρ_f/ρ_d and ρ_a/ρ_d are the film-drop and air-drop density ratios. For simplification, we use $\rho_f/\rho_d = 1$ (also see table 1). In order to keep the surrounding medium as air, ρ_a/ρ_d and Oh_a are fixed at 10^{-3} and 10^{-5} , respectively. We also fix the Bond number (ratio of the gravitational to the capillary pressure) given by

$$Bo_d = \frac{\rho_d g R^2}{\gamma} \quad (2.9)$$

at 0.5 during this study. The initial condition (figure 1b) is given by the normalized impact velocity, $\tilde{V} = \sqrt{We_d}$.

Lastly, a singular body force \tilde{f}_γ is applied at the interfaces to respect the dynamic boundary condition across them. The approximate forms of these forces follow from Brackbill *et al.* (1992); Prosperetti & Tryggvason (2009); Tryggvason *et al.* (2011) as

$$\tilde{f}_\gamma \approx \tilde{\kappa}_1 \tilde{\nabla} \Psi_1 + \tilde{\kappa}_2 \tilde{\nabla} \Psi_2. \quad (2.10)$$

Here, κ_1 and κ_2 are the curvatures associated with Ψ_1 and Ψ_2 , respectively, calculated using the height-function method. During the simulations, the maximum time-step needs to be set less than the oscillation period of the smallest wavelength capillary wave as the surface-tension scheme is explicit in time (Popinet 2009; Popinet & Collaborators 2013–2022b).

Figure 1(b) represents the axi-symmetric computational domain. A tangential stress-free and non-penetrable boundary condition is applied on each of the domain boundaries. The pressure gradient is also set to zero at these boundaries. Furthermore, the domain boundaries are chosen to be far enough not to influence the drop impact process. When $Oh_f > 0.1$ and waves on the film are damped, we choose $\mathcal{L}_{\max} = 8R$. The cases with low Oh_f require extra attention due to the train of surface waves formed post-impact as these waves can reflect back from the side-walls (here, we choose $\mathcal{L}_{\max} \gg 8R$).

3. Phenomenology of the impact events

In figure 2, we compare the behavior of a typical silicone oil drop ($R = 1.0$ mm, $V = 0.35$ m/s, and $\eta_d = 4.6$ mPa.s, i.e. (We_d, Oh_d, Bo_d) = (4, 0.034, 0.5)) impacting on films with a fixed viscosity $\eta_f = 96$ mPa.s ($Oh_f = 0.67$) but contrasting thicknesses: $h_f = 0.01, 0.35$, and 0.85 mm (i.e. $\Gamma = 0.01, 0.35$, and 0.85 , respectively). We show a one-to-one comparison between experimental and DNS snapshots, and display three key pieces of information: the position of the liquid-air interfaces (green lines) that can be directly compared with experiments, the rate of viscous dissipation per unit volume (left panel of each numerical snapshot), and the magnitude of the velocity field (right panel of each numerical snapshot).

For the thinnest film ($h_f = 0.01$ mm, figure 2a and supplementary video SM1), the drop

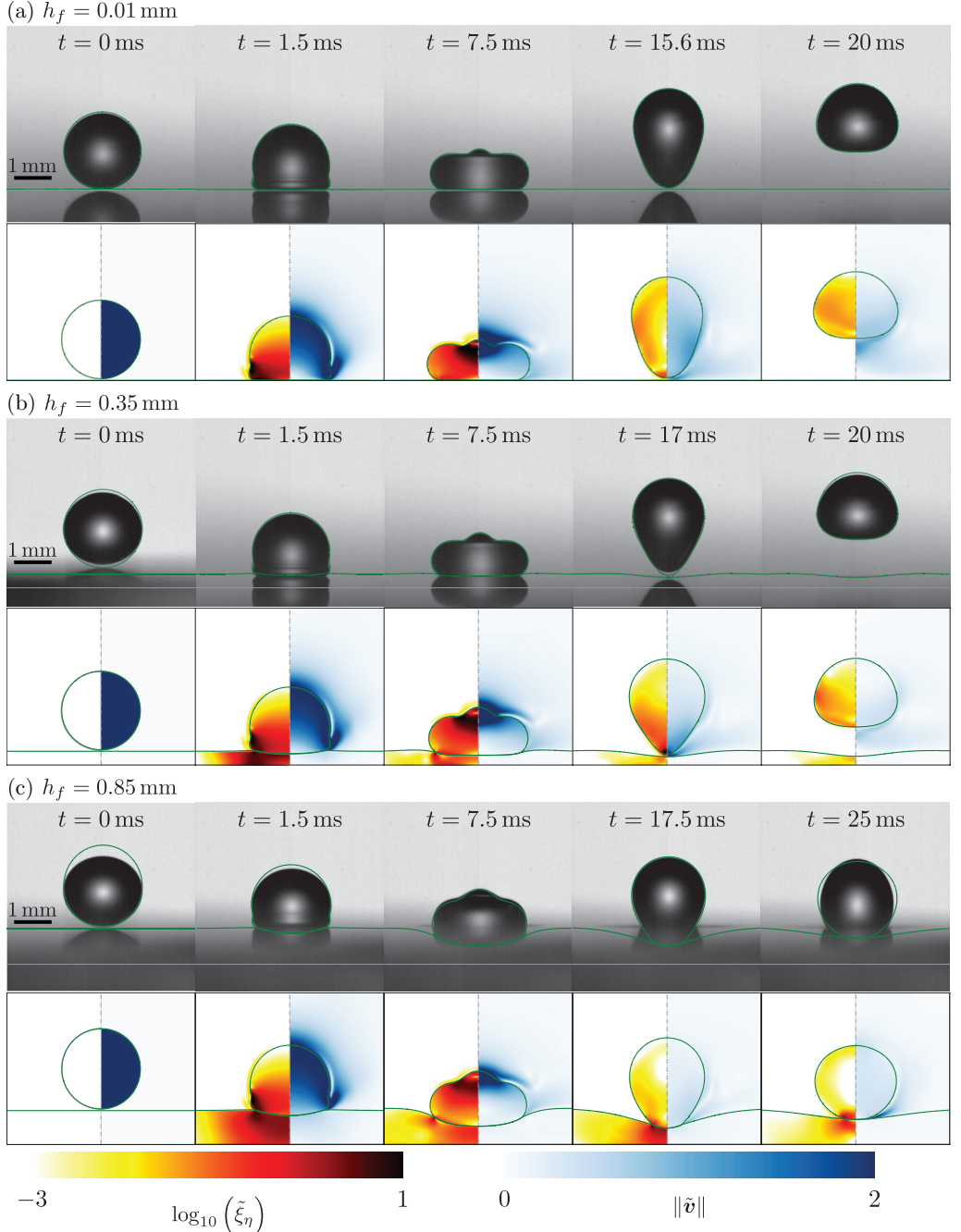


FIGURE 2. Effect of the film thickness on the drop impact process: comparison of the experimental and DNS snapshots of the impact process on films with h_f = (a) 0.01 mm, (b) 0.35 mm, and (c) 0.85 mm. In each panel, the top row contains the experimental images with (green) interface outline from DNS, and the bottom row contains numerical snapshots showing the dimensionless rate of viscous dissipation per unit volume ($\tilde{\xi}_\eta = 2Oh(\tilde{\mathcal{D}} : \tilde{\mathcal{D}})$) on the left and the magnitude of dimensionless velocity field (\tilde{v}) on the right. We show $\tilde{\xi}_\eta$ on a \log_{10} scale to identify regions of maximum dissipation (marked with black for $\tilde{\xi}_\eta \geq 10$). For all cases in this figure, $R = 1 \text{ mm}$, $V = 0.3 \text{ m/s}$, $\eta_d = 4.6 \text{ mPa.s}$ and $\eta_f = 96 \text{ mPa.s}$, corresponding to $(Wed, Oh_d, Oh_f) = (4, 0.034, 0.67)$. Videos SM1–SM3 are available in the supplementary material at X.

deforms as it comes in apparent contact with the film mediated by the air layer, an instant that we choose as the origin of time $t = 0$. The drop spreads until it reaches its maximal lateral extent, recoils and rebounds in an elongated shape after a time $t_c = 15.6 \pm 0.1$ ms, called the contact time. Throughout the impact process, viscous stresses inside the drop dissipate energy (see times $t = 1.5$ ms and 7.5 ms). Consequently, after take off, the drop reaches a maximal center of mass height $H = 2.0 \pm 0.1$ mm relative to the undisturbed film surface, from which we deduce the restitution coefficient defined as $\varepsilon = \sqrt{2g(H - R)}/V$, here $\varepsilon = 0.48 \pm 0.05$. The liquid-air interface profiles obtained from experiments and numerics are in excellent agreement, and we measure the same value of the contact time and restitution coefficient in simulations, using the method described in appendix E. This behavior is in quantitative agreement with that reported for the impact of a viscous drop on a superhydrophobic surface by Jha *et al.* (2020), suggesting that the presence of both the air and liquid film have a negligible influence on the macroscopic dynamics of the rebound, and that viscous dissipation in the drop determines the rebound height.

For $h_f = 0.35$ mm (figure 2b and supplementary video SM2), despite the noticeable deformation of the liquid film, the qualitative features of the bounce are similar. We further observe that as the drop takes off, the film free surface has not yet recovered its undisturbed position. We measure an increase of the contact time to $t_c = 17 \pm 0.1$ ms and a decrease in the rebound elasticity, with $H = 1.6 \pm 0.1$ mm implying $\varepsilon = 0.37 \pm 0.04$. The DNS snapshots show that in this case, viscous dissipation occurs both in the drop and the underlying liquid. Qualitatively, the instantaneous rate of viscous dissipation in the drop is similar for $h_f = 0.01$ mm and $h_f = 0.35$ mm, suggesting that the decrease in rebound elasticity is primarily linked to the increased film dissipation.

Finally, for $h_f = 0.85$ mm (figure 2c and supplementary video SM3), the film deformation increases and the substrate loses its repellent ability. The drop center of mass does not take off above $H = R$, the drop floats on top of the liquid film, a situation that corresponds to the inhibition of bouncing for which $\varepsilon \approx 0$ and the contact time diverges. In this case, we notice that the experimental and numerical interface profiles differ at $t = 0$ ms. This initial discrepancy, caused by drop oscillations upon detachment from the needle, does not affect the subsequent impact dynamics and the impact outcome, as evidenced by the good agreement of the interface profiles at later instants.

We now systematically vary the film thickness h_f while keeping the drop and film viscosities constant ($\eta_d = 4.6$ mPa.s and $\eta_f = 96$ mPa.s) and plot, in figures 3(a) and (b), the contact time t_c and the coefficient of restitution ε extracted from experiments (circles) and DNS (hexagrams). Experiments and simulations are in excellent agreement when varying the film thickness by two orders of magnitude, $h_f = 0.01$ mm – 1 mm. The existence of two regimes is readily apparent. Firstly, for $h_f \lesssim 0.1$ mm, both t_c and ε are independent of h_f . The value of the contact time in this regime, $t_c = 15.6 \pm 0.5$ ms, corresponds to that expected from the inertio-capillary scaling (Wachters & Westerling 1966; Richard *et al.* 2002). The contact time is proportional to $\tau_\gamma = \sqrt{\rho_d R^3/\gamma}$ with a prefactor 2.2 ± 0.1 , in good agreement with that calculated by Rayleigh (1879) for the fundamental mode of drop oscillation $\pi/\sqrt{2}$. Similarly, the plateau value of the coefficient of restitution $\varepsilon = 0.47 \pm 0.04$ is in reasonable agreement with that reported for the impact of water drops on superhydrophobic substrates for similar drop Ohnesorge number Oh_d and impact Weber number We_d (Jha *et al.* 2020). We therefore refer to this regime as substrate-independent rebound (see also appendix B).

Secondly, for $h_f \gtrsim 0.1$ mm, the contact time and coefficient of restitution are influenced by the film thickness. We observe that t_c increases (figure 3a) and ε decreases (figure 3b) with increasing h_f until t_c diverges and bouncing ceases ($\varepsilon = 0$) for $h_f \approx 0.75$ mm. This critical thickness marks the threshold of the rebound behavior and the transition to the

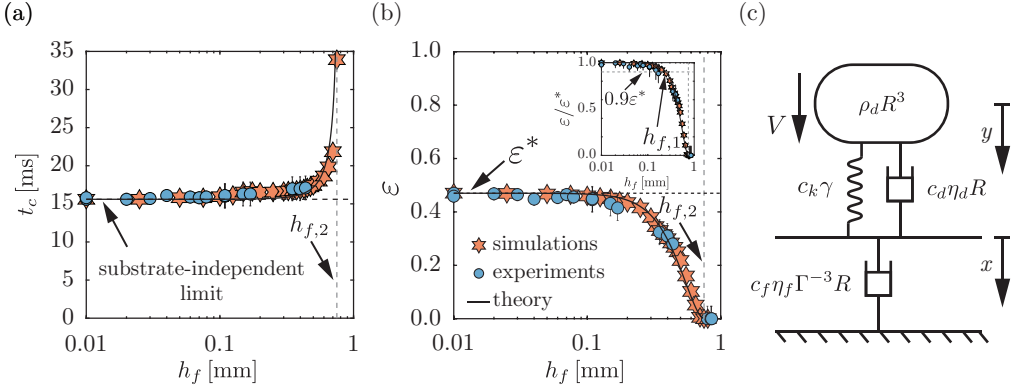


FIGURE 3. Effect of the film thickness on the rebound characteristics for $R = 1$ mm, $V = 0.3$ m/s, $\eta_d = 4.6$ mPa.s and $\eta_f = 96$ mPa.s, i.e. (We_d, Oh_d, Oh_f) = (4, 0.034, 0.67): (a) contact time t_c and (b) restitution coefficient ε as a function of film thickness h_f . Circles and hexagrams represent experiments and DNS, respectively. In panels (a) and (b), the horizontal black dashed lines represent the substrate-independent limits of contact time and restitution coefficient, respectively, while the solid black lines shows the results from the phenomenological model (see § 4) with parameters $c_k = 2$, $c_d = 5.6$ and $c_f = 0.46$. The vertical gray dotted line marks the transition from the bouncing to the non-bouncing (floating) regime. The inset of panel (b) illustrates the variation of the restitution coefficient normalized by its substrate-independent value ε^* as a function of the film thickness. Here, the horizontal gray line represents $\varepsilon = 0.9\varepsilon^*$, marking the transition from substrate-independent to substrate-dependent bouncing at $h_f = h_{f,1}$. (c) Schematic diagram of the phenomenological model that describes the drop impact process on a liquid film. The parameters $\rho_d R^3$, $\eta_d R$, and γ are associated to the drop properties and $\eta_f \Gamma^{-3} R$ is associated to the film properties.

non-bouncing (floating) regime. Here, the rebound characteristics vary significantly with h_f and we therefore refer to this regime as substrate-dependent.

Finally, we characterize the transition from the substrate-independent to the substrate-dependent regime by introducing the thickness $h_{f,1}$, in dimensionless form $\Gamma_1 = h_{f,1}/R$, which marks the decrease of ε to 0.9 times its plateau value ε^* . Similarly, we define the critical thickness $h_{f,2}$, respectively $\Gamma_2 = h_{f,2}/R$, associated to the transition from the substrate-dependent to the non-bouncing (floating) regime as the smallest film thickness which results in $\varepsilon = 0$. The impact dynamics can be categorized into three distinct regimes: a substrate-independent regime for $\Gamma = h_f/R \leq \Gamma_1$, a substrate-dependent regime for $\Gamma_1 < \Gamma < \Gamma_2$, and a non-bouncing (floating) regime for $\Gamma \geq \Gamma_2$.

4. Phenomenological model

We now seek to rationalize the dependence of the rebound time and elasticity with the substrate and drop properties by constructing a minimal model, guided by our experimental and numerical observations. We build on the classical description of a drop as a liquid spring which reflects the balance of inertia and capillarity during a rebound (Richard *et al.* 2002; Okumura *et al.* 2003). Here, we consider viscous drops and further add a damping term to the liquid spring, an approach which has been shown to successfully capture the variation of contact time and coefficient of restitution across over two orders of magnitude variation in liquid viscosities (Jha *et al.* 2020). Similarly, we interpret the film behavior through the liquid spring analogy. The film motion contrasts with that of the drop, while the latter displays a full cycle of oscillation during a rebound,

the former never returns to its undisturbed position (see figure 2 and supplementary movies SM1 - SM3). This observation leads us to consider that the damping component dominates the behavior of the liquid film, and to neglect the contributions of inertia and surface tension. We further discuss this assumption and its validity in § 6.

In figure 3(c), we present a sketch of the model, where we assume that the droplet and the film are connected in series during apparent contact, and show the scaling forms of the drop and film components. The scaling relations for the drop mass, stiffness and damping are taken from the work of [Jha et al. \(2020\)](#) as proportional to $\rho_d R^3$, γ , and $\eta_d R$, respectively, with corresponding prefactors of 1, c_k , and c_d . We determine the values of c_k and c_d from results in the substrate-independent bouncing regime (see appendix B). The scaling form of the film damping term is chosen as proportional to $\eta_f \Gamma^{-3} R$, where $\Gamma = h_f/R$, with corresponding prefactor of c_f (figure 3c). This is built on two key assumptions. First, we assume that the lubrication approximation holds in the film as, for sufficiently high film Ohnesorge numbers ($Oh_f \gtrsim 0.1$), the slopes associated to the film deformations are small ($\Gamma \ll 1$, $Oh_f \sim \mathcal{O}(1)$, see § 6 for limitations). And second, we choose to consider the drop as an impacting disk rather than a sphere, owing to the rapid drop spreading upon impact ([Eggers et al. 2010](#); [Wildeman et al. 2016](#)), which results in a damping term proportional to Γ^{-3} instead of Γ^{-1} ([Leal 2007](#)). Lastly, we fit the prefactor c_f to our experiments and simulations.

With these assumptions, the equations of motion for the model system (figure 3c) read

$$\rho_d R^3 \ddot{y} = -c_k \gamma (y - x) - c_d \eta_d R (\dot{y} - \dot{x}), \quad (4.1)$$

$$0 = +c_k \gamma (y - x) + c_d \eta_d R (\dot{y} - \dot{x}) - c_f \eta_f \Gamma^{-3} R \dot{x}, \quad (4.2)$$

where y and x are the displacements of the drop and the film relative to their initial position in the reference frame of the laboratory, and the dots denote time derivatives. We point out that by setting $\dot{x} = x = 0$, we recover the model proposed by [Jha et al. \(2020\)](#), which extends the analogy between the drop impact process and a spring-mass system ([Okumura et al. 2003](#)) by adding a damper to account for viscous dissipation in the drop. Here, we additionally consider viscous dissipation in the liquid coating and model the film as a damper without inertia. We make this modelling assumption, guided by the overdamped dynamics of the film (figure 2), to keep the number of free parameters to as few as possible (three in the present study, c_k , c_d , and c_f). We stress here that c_k and c_d are fixed in this study, and that their value is in quantitative agreement with the corresponding prefactors derived by [Jha et al. \(2020\)](#).

Similarly as for the governing equations in DNS, we make equations (4.1) and (4.2) dimensionless using the length scale R and the time scale τ_γ and use tildes to identify dimensionless variables. Next, we obtain an equation of motion for the drop deformation $\tilde{z} = \tilde{y} - \tilde{x}$, namely

$$\left(1 + \frac{c_d Oh_d}{c_f Oh_f \Gamma^{-3}}\right) \ddot{\tilde{z}} + c_d Oh_d \left(1 + \frac{c_k}{c_d Oh_d \cdot c_f Oh_f \Gamma^{-3}}\right) \dot{\tilde{z}} + c_k \tilde{z} = 0, \quad (4.3)$$

which admits oscillatory solutions, that is drop rebound, under the condition

$$\omega^2 = 4c_k - \left(c_d Oh_d - \frac{c_k}{c_f Oh_f \Gamma^{-3}}\right)^2 > 0. \quad (4.4)$$

We note that ω^2 decreases with increasing Γ for fixed Oh_d and Oh_f , in qualitative agreement with the existence of a critical film height above which bouncing stops (figure

321 3b). Equation (4.4) allows us to determine the bounds of the bouncing regime in terms of
 322 a critical drop Ohnesorge number $Oh_{d,c}$ and film thickness Γ_2 . Discarding the two roots
 323 of the equation $\omega^2 = 0$ that yield unphysical negative values of $Oh_{d,c}$ and Γ_2 , we obtain

$$324 \quad Oh_{d,c} = \frac{1}{c_d} \left(2\sqrt{c_k} + \frac{c_k}{c_f} \left(\Gamma_2/Oh_f^{1/3} \right)^3 \right), \text{ and} \quad (4.5)$$

$$325 \quad \Gamma_2/Oh_f^{1/3} = \left(\frac{c_f}{c_k} (c_d Oh_d + 2\sqrt{c_k}) \right)^{1/3}. \quad (4.6)$$

326 Equations (4.4)–(4.6) evidence that the role of the film viscosity and height are inter-
 327 twined as we find the combination $\Gamma/Oh_f^{1/3}$ that can be inferred as the effective film
 328 thickness or mobility. Furthermore, the substrate-independent bouncing threshold is
 recovered when this film mobility, $\Gamma/Oh_f^{1/3}$, tends to 0, that is for very thin and/or very
 viscous films. Indeed, equations (4.5)–(4.6) become

$$329 \quad Oh_{d,c} = \frac{2\sqrt{c_k}}{c_d}, \text{ and} \quad (4.7)$$

$$330 \quad \Gamma_2/Oh_f^{1/3} = \left(2 \frac{c_f}{\sqrt{c_k}} \right)^{1/3}, \quad (4.8)$$

331 for the limiting cases of substrate-independent ($\Gamma/Oh_f^{1/3} \rightarrow 0$), and inviscid drop
 332 ($Oh_d \rightarrow 0$) asymptotes, respectively.

333 To go further, we solve equation (4.3) with the initial conditions $\tilde{z} = 0$ and $\dot{\tilde{z}} = \sqrt{We_d}$
 334 at $\tilde{t} = 0$, yielding

$$335 \quad \tilde{z}(\tilde{t}) = \frac{2\sqrt{We_d}}{\Omega} \exp \left(-\frac{\phi \tilde{t}}{2} \right) \sin \left(\frac{\Omega \tilde{t}}{2} \right), \quad (4.9)$$

$$336 \quad \text{where } \phi = \frac{c_k + c_d Oh_d c_f Oh_f \Gamma^{-3}}{c_d Oh_d + c_f Oh_f \Gamma^{-3}} \quad (4.10)$$

$$337 \quad \text{and } \Omega = \omega \left(1 + \frac{c_d Oh_d}{c_f Oh_f \Gamma^{-3}} \right)^{-1} \quad (4.11)$$

338 can be interpreted as an effective damper and angular frequency, respectively, by com-
 339 paring the above expression to the one obtained by Jha *et al.* (2020) for $\Gamma/Oh_f^{1/3} \rightarrow 0$.
 340 We can deduce the expressions for both the contact time and the coefficient of restitution
 341 using these pieces of information. The contact time is taken as the instant at which the
 342 drop deformation \tilde{z} comes back to zero, which occurs at $\Omega \tilde{t} = 2\pi$, giving

$$343 \quad \frac{t_c}{\tau_\gamma} = \frac{2\pi}{\omega} \left(\frac{c_d Oh_d}{c_f Oh_f \Gamma^{-3}} + 1 \right). \quad (4.12)$$

344 Equation (4.12) is then used to compute the coefficient of restitution ε as the ratio
 345 of rebound velocity, $\dot{\tilde{z}}(\tilde{t}_c)$, to the impact velocity, $\sqrt{We_d}$. We immediately notice that
 346 this definition yields an expression for ε that does not depend on We_d , in contrast
 347 with the experimentally observed decrease of ε with We_d . We account for the Weber
 348 number dependence of ε , which is not captured by spring mass models (Jha *et al.* 2020),
 349 by scaling the coefficient of restitution by $\varepsilon_0(We_d)$, its We_d -dependent value in the
 350 substrate-independent limit for inviscid drops,

$$\varepsilon(We_d, Oh_d, Oh_f, \Gamma) = \varepsilon_0(We_d) \exp\left(-\frac{\pi}{\omega} \left(c_d Oh_d + \frac{c_k}{c_f Oh_f \Gamma^{-3}}\right)\right), \quad (4.13)$$

where the prefactor $\varepsilon_0(We_d)$ is not a model prediction. We obtain the other prefactors, c_k & c_d by fitting the substrate-independent experiments following [Jha et al. \(2020\)](#). This simplification allows us to recover the expressions for t_c and ε for viscous drop impact on non-wetting substrates ([Jha et al. 2020](#)), and thus to determine $c_k = 2$ and $c_d = 5.6$ which we keep fixed during this study. For details of this simplification and on the determination of the prefactors, see appendix B.

We test the model predictions for the contact time and rebound elasticity in the substrate-dependent regime by comparing the data (symbols) presented in figures 3(a) and (b) to least-square fits of equations (4.12) and (4.13) with c_f as a free parameter (solid lines) and taking $\varepsilon_0 = 0.58$ (see appendix B). We find that the model accurately predicts the variation of t_c and ε with Γ for $c_f = 0.46 \pm 0.1$. For the rest of this work, we fix $c_f = 0.46$ and assess the predictive ability of the simplified model.

5. Influence of drop and film parameters

We now test the model predictions and limits by experimentally and numerically varying the drop and film Ohnesorge numbers. We give particular attention to the value of the coefficient c_f (fixed at 0.46) necessary to fit the model to this data, and to the two asymptotes predicted by the model that bound the bouncing domain (equations (4.7)-(4.8)).

5.1. Influence of the film Ohnesorge number Oh_f

We first vary the film Ohnesorge number Oh_f while keeping the drop and impact properties constant. In figure 4(a), we show the evolution of the coefficient of restitution ε for drops with $Oh_d = 0.034$ as a function of the dimensionless film thickness Γ while exploring two decades in film viscosity, $Oh_f = 0.01 - 2.0$. On the one hand, as expected, the values of the coefficient of restitution are not affected in the substrate-independent limit. On the other hand, the substrate-dependent behavior shows the influence of Oh_f and we identify two regimes. For $Oh_f < 0.1$, the evolution of ε with Γ does not depend on Oh_f , as illustrated by the data collapse in figure 4(a). However, for $Oh_f > 0.1$, increasing the film viscosity leads to a larger extent of the substrate-independent plateau and to an increase of the critical film thickness at which bouncing stops. This change in the Oh_f dependence can be characterized by the two dimensionless critical film thicknesses $\Gamma_1 = h_{f,1}/R$, and $\Gamma_2 = h_{f,2}/R$, which increase from 0.17 to 0.33 and 0.58 to 1.1, respectively, when Oh_f is increased from 0.1 to 2.0.

We interpret the two types of behavior in the substrate-dependent regime in the light of our minimal model, which predicts that the film mobility, $\Gamma/Oh_f^{1/3}$, controls the dissipation in the substrate. In figure 4(b), we plot the coefficient of restitution data presented in (a) after rescaling the horizontal axis by $Oh_f^{-1/3}$. The data now collapse for $Oh_f > 0.1$, indicating that the proposed approximations capture the large viscosity limit but breaks down for lower film Ohnesorge numbers. We further evidence the validity and failure of the minimal model by plotting the predictions of equation (4.13) with $c_f = 0.46$ (dashed colored lines in figure 4a and solid black line in figure 4b). The minimal model predicts the restitution coefficient accurately for $Oh_f > 0.1$, suggesting that our modelling assumptions are valid in this regime: the liquid film dynamics is

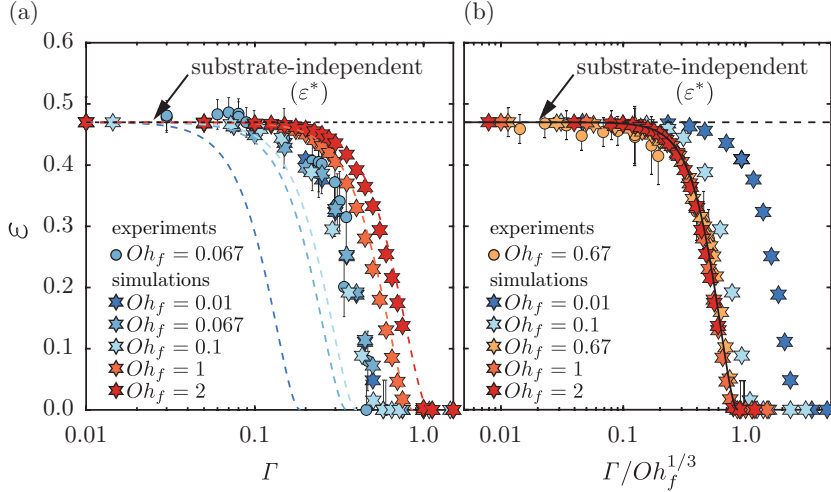


FIGURE 4. Influence of the film parameters on the impact characteristics: variation of the coefficient of restitution ε as a function of (a) the film thickness Γ and (b) the film mobility $\Gamma/Oh_f^{1/3}$. In panels (a) and (b), the circles and hexagons correspond to the results from experiments and simulations, respectively. The colored dashed lines in panel (a) and the solid black line in panel (b) illustrate the results from the phenomenological model (equation (4.13)) with parameters $c_k = 2$, $c_d = 5.6$ and $c_f = 0.46$. Black dashed lines in panels (a) and (b) mark the substrate-independent limit of the restitution coefficient ε^* . For all cases in this figure, $Oh_d = 0.034$ and $We_d = 4$.

387 dominated by viscous dissipation, and the flow can be successfully modelled in the
388 lubrication approximation by assimilating the impacting drop to a cylinder.

389 5.2. Influence of the drop Ohnesorge number Oh_d

390 In this section, we focus on the influence of the drop Ohnesorge number on the
391 rebound elasticity. In figure 5(a), we plot the coefficient of restitution as a function of the
392 dimensionless film thickness for a fixed $Oh_f = 0.667$ and for varying Oh_d spanning
393 the range $0.01 - 0.133$. Increasing Oh_d affects ε across all film thicknesses. In the
394 substrate-independent region, the coefficient of restitution decreases with increasing
395 drop Ohnesorge number. In appendix B, we show that the plateau values reported in
396 figure 5(a) decay exponentially with increasing Oh_d as predicted by Jha *et al.* (2020). To
397 better illustrate the influence of Oh_d in the substrate-dependent regime, we normalize
398 the coefficient of restitution ε by its substrate-independent value ε^* (figure 5b). With
399 this normalization, we expect the data to follow the prediction of equation (4.13) (solid
400 line). The data collapse only for small Γ , indicating that the phenomenological model
401 predicts the influence of Oh_d only in the substrate-independent limit. This suggests that
402 the model fails to account for the interplay between the drop and the film properties that
403 affects dissipation in both liquids, and ultimately the coefficient of restitution. Here as
404 well, we monitor the Oh_d dependence of the coefficient of restitution, and its deviation
405 from the prediction of equation (4.13), through the evolution of Γ_1 and Γ_2 , that both
406 decrease with increasing Ohnesorge number.

407 5.3. Influence of Oh_f and Oh_d on the critical film thicknesses

408 We now quantify the influence of the drop and film Ohnesorge number by reporting
409 their effect on the critical thicknesses for substrate-independent to substrate-dependent
410 (Γ_1) and bouncing to non-bouncing (floating) (Γ_2) transitions. Indeed, we have shown

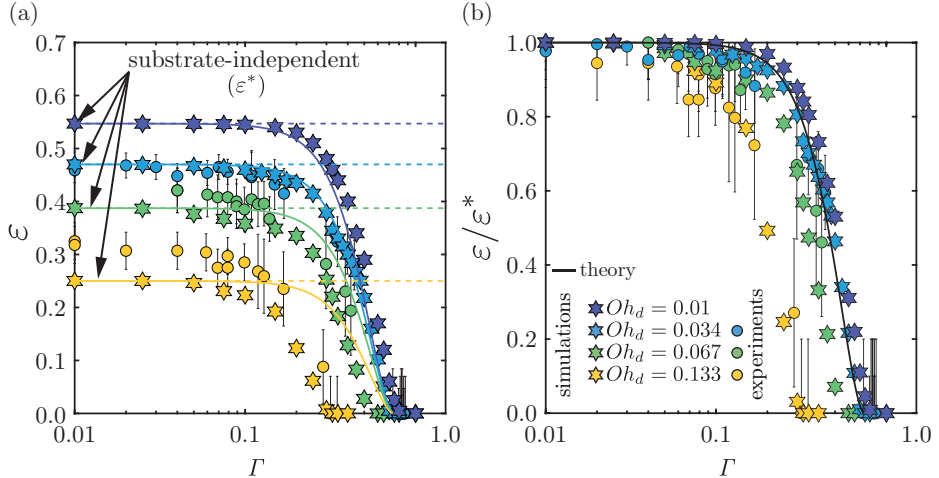


FIGURE 5. Influence of the drop parameters on the rebound elasticity: variation of (a) the coefficient of restitution ε and (b) the coefficient of restitution normalized with its substrate-independent value $\varepsilon/\varepsilon^*$ as a function of the normalized film thickness Γ . The circles and hexagrams correspond to the results from the experiments and simulations, respectively. In panel (a), the dashed lines denote the plateau values of the restitution coefficient $\varepsilon^*(Oh_d)$. In panels (a) and (b), the solid lines represent the results from the phenomenological model (equation (4.13)) with parameters $c_k = 2$, $c_d = 5.6$ and $c_f = 0.46$. For all cases in this figure, $Oh_f = 0.667$ and $Wed = 4$.

above that these two critical thicknesses are good proxies to characterize the continuous transition from substrate-independent bouncing to rebound inhibition. In figures 6(a,b), we show Γ_1 and Γ_2 as a function of the film Ohnesorge number for Oh_d in the range 0.01–0.133. This representation reflects the existence of the two distinct regimes reported in figure 4.

First, when $Oh_f < 0.1$, Γ_1 and Γ_2 are independent of Oh_f . We write $\Gamma_1 = \alpha_1(Oh_d)$ and $\Gamma_2 = \alpha_2(Oh_d)$, and report the values of $\alpha_1(Oh_d)$ and $\alpha_2(Oh_d)$ in figures 6(c,d). This observation is in contradiction with the expectations from our minimal model which predicts that Oh_f influences the values of Γ_1 and Γ_2 . Surprisingly, this Oh_f -independence of the critical thicknesses and the collapse observed in figure 4(a) suggest that the energy transfer to the film (in the form of kinetic and surface energies) and the film viscous dissipation are independent of film viscosity for $Oh_f < 0.1$. We will further elaborate on this regime in § 6.

Second, for larger film Ohnesorge numbers, the dissipation in the film is captured by the lubrication approximation ansatz. As a result, both critical thicknesses follow the relations $\Gamma_1 = \beta_1(Oh_d)Oh_f^{1/3}$ and $\Gamma_2 = \beta_2(Oh_d)Oh_f^{1/3}$, as predicted by the model. Beyond this scaling relation, the accuracy of the minimal model is tied to its ability to predict the prefactors β_1 and β_2 when $Oh_f \gtrsim 0.1$. In figures 6(c,d), we plot β_1 and β_2 as a function of the drop Ohnesorge number. Both prefactors show a plateau for $Oh_d \lesssim 0.03$ before decreasing monotonically with the drop Ohnesorge number. We compare the measured prefactors to the model predictions which we plot as a solid lines in figures 6(c,d). β_1 is obtained by solving $\varepsilon = 0.9\varepsilon^*$, yielding

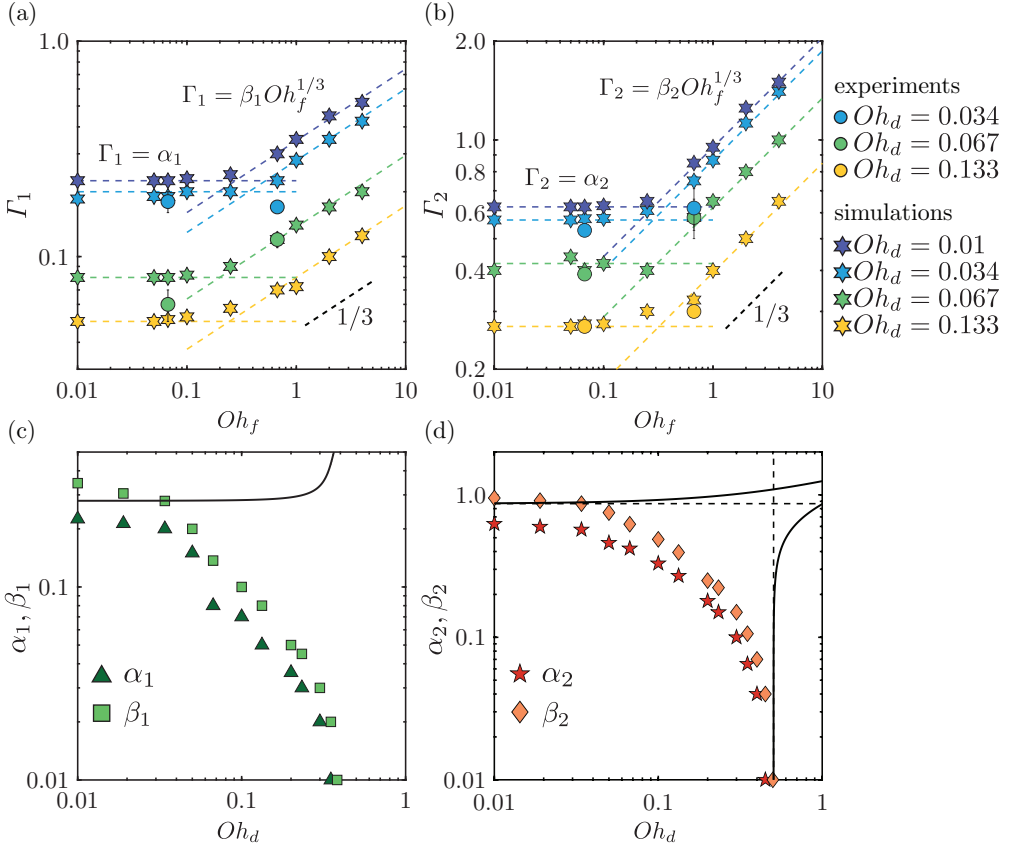


FIGURE 6. Critical film thickness marking the transition from (a) substrate-independent to substrate-dependent bouncing Γ_1 and (b) bouncing to non-bouncing (floating) Γ_2 as a function of Oh_f at different Oh_d . Prefactors (c) α_1 and β_1 , and (d) α_2 and β_2 as a function of Oh_d . The solid black line in panel (c) represents the model prediction for β_1 , equation (5.1). The solid black lines in panel (d) represent the model predictions for β_2 using equations (4.5)-(4.6), and the black dashed lines show the two asymptotes, equations (4.7)-(4.8).

$$\beta_1 = c_f^{1/3} \left[\frac{-c_d Oh_d(1 - r^2) + 2r\sqrt{c_k(1 + r^2) - c_d^2 Oh_d^2}}{c_k(1 + r^2)} \right]^{1/3}, \quad (5.1)$$

$$\text{where, } r = \frac{c_d Oh_d}{\sqrt{4c_k - c_d^2 Oh_d^2}} - \frac{\ln(0.9)}{\pi}, \quad (5.2)$$

and β_2 is given by equation (4.6). The model fails to capture both the decrease of β_1 and β_2 with Oh_d . Yet, we can interpret the evolution of these two prefactors along the inviscid and viscous drop limiting cases. Indeed, for inviscid drops (*i.e.* small Oh_d), the model predictions for β_1 and β_2 show a plateau whose value is in good agreement with that reported in experiments. Conversely, for viscous drops (*i.e.* large Oh_d), β_2 decreases with Oh_d to match the asymptote associated to the substrate-independent bouncing inhibition occurring at $Oh_{d,c} \approx 0.5$ (equation (4.5) and dotted line in figure 6d).

We stress that the model predictions shown in figures 6(c,d) consider a unique value

of $c_f = 0.46 \pm 0.1$, determined from least-square fit in § 4. We attribute the failure of the model to predict the dependence on Oh_d away from the two asymptotes to its simplified representation of the drop–film interactions. While these oscillator based models remarkably predict the global outcome of a rebound, that is, for example, the contact time, coefficient of restitution, and the bounds of bouncing, they fail at accurately representing the interactions, such as the drop or film deformations (equation (4.9)), and their dynamics. For example, the force associated to drop impact is maximal at early times, when the drop shape is spherical, while the force exerted by a spring is proportional to deformation.

Our phenomenological model successfully captures the behavior of the liquid film for $Oh_f \geq 0.1$, giving support to the modeling assumptions. Within this regime, the model allows for a quantitative prediction of the contact time and coefficient of restitution for both inviscid (*i.e.* low Oh_d) and viscous (*i.e.* large Oh_d) drops, for a fixed set of constants c_k , c_d and c_f . In between these two limits, the model fails to predict the Oh_d dependence, a fact we attribute to the simplicity of the representation of drop-film interactions. More intriguingly, the minimal model also breaks down for $Oh_f \lesssim 0.1$, where we observe that the coefficient of restitution does not depend on the film Ohnesorge number. We will demystify this behavior in the next section.

6. Bouncing inhibition on low Ohnesorge number films

We now investigate the independence of the rebound elasticity with the film Ohnesorge number, illustrated by the data collapse of figure 4(a), for $Oh_f < 0.1$. Figure 7(a) shows two typical impact scenarios in this regime, with $Oh_f = 0.01$ (figure 7(a - i)) and 0.1 (figure 7(a - ii)), where bouncing is inhibited by the presence of the liquid film. Although these two representative cases differ by an order of magnitude in Oh_f , qualitatively, the drop shape and flow anatomy remain similar (figure 7a, $t/\tau_\gamma = 0.2, 1$), suggesting an equal loading on the film. Nonetheless, the film response varies. We observe surface waves post impact on the film-air interface for $Oh_f = 0.01$, which vanish for $Oh_f = 0.1$ owing to increased bulk viscous attenuation (figure 7a, $t/\tau_\gamma = 0.2, 2.65$).

To further elucidate the drop–film interaction, we compute the energy budgets associated to the two representative cases with $Oh_f = 0.01$ (figure 7(b - i)) and 0.1 (figure 7(b - ii)). The overall energy budget reads

$$E_0 = (E_k^d + \Delta E_\gamma^d + \Delta E_g^d) + E_\eta^d + (E_k^f + \Delta E_\gamma^f + \Delta E_g^f) + E_\eta^f + E_t^a, \quad (6.1)$$

where E_0 is the energy at impact (*i.e.*, the sum of the drop’s kinetic and gravitational potential energies). The subscripts g, k, γ , and η denote gravitational potential, kinetic, surface, and viscous dissipation energies, respectively. Moreover, the superscripts d, f , and a represent drop, film and air, respectively. Lastly, reference values to calculate ΔE_g and ΔE_γ are at minimum E_g , and E_γ , at $t = 0$, respectively. Note that the contribution of the total energy associated with air ($E_t^a = E_k^a + E_\eta^a$) is negligible compared to other energies ($E_t^a(t/\tau_\gamma = 4) \approx 0.01E_0$). Readers are referred to Landau & Lifshitz (1987); Wildeman *et al.* (2016); Ramírez-Soto *et al.* (2020); Sanjay *et al.* (2022b) for details of energy budget calculations.

In both cases, the magnitude of the drop energy (the sum of the drop’s kinetic, gravitational potential and surface energies) at the end of the rebound cycle, that is for $t = 3.25\tau_\gamma$ when $Oh_f = 0.01$ and $t = 2.65\tau_\gamma$ when $Oh_f = 0.1$ (vertical grey dashed lines), is similar, as expected from the independence of ε with Oh_f . Note that the end of

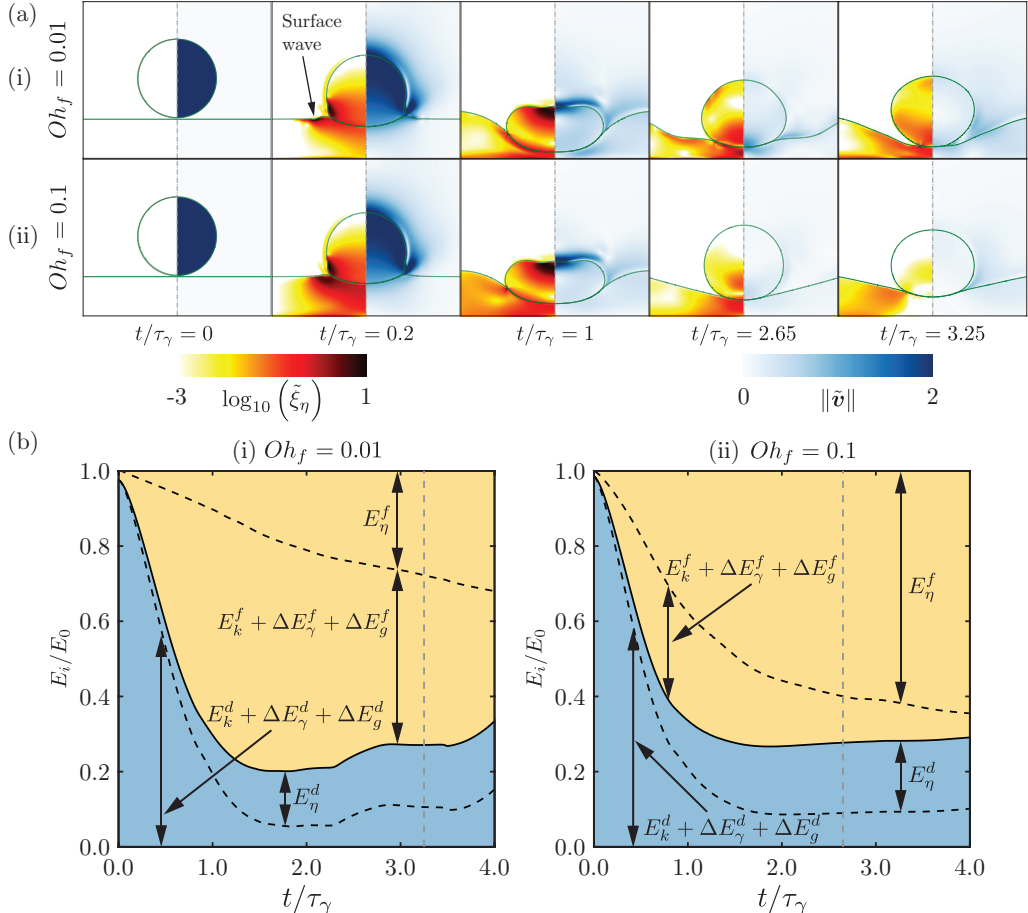


FIGURE 7. Oh_f independent inhibition of bouncing: (a) typical drop impact dynamics on low viscosity films. The snapshots show the dimensionless rate of viscous dissipation per unit volume on the left and the magnitude of dimensionless velocity field on the right. (b) Energy budgets for the two representative cases shown in panel (a), normalized by the available energy at the instant of impact. Here, the subscripts g , k , γ , and η denote gravitational potential, kinetic, surface, and viscous dissipation energies, respectively. The superscripts d , f , and a represent drop, film and air, respectively. The grey dashed line in each panel marks the instant when the normal reaction force between the drop and the film is minimum and represents the last time instant when the drop could have bounced off the film. In each panel, $Oh_f =$ (i) 0.01 and (ii) 0.1. For all the cases, We_d , Oh_d , $\Gamma = 4, 0.034, 1$.

the cycle has been determined from the instant at which the reaction force between the drop and the film is minimum (see appendix E and Zhang *et al.* 2022). Moreover, the energy budget evidences that the viscous dissipation in the drop during the rebound is similar, indicating that the magnitude of the energy transferred from the impacting drop to the film (the sum of the film's kinetic, gravitational potential and surface energies, and viscous dissipation) is not affected by the one order of magnitude change in Oh_f . Yet, the distribution of the film energy is dramatically different in the two cases we consider. For $Oh_f = 0.1$, the energy transferred to the film is mostly lost to viscous dissipation, while for $Oh_f = 0.01$ the energy stored in the film's kinetic, surface and potential components dominates. We stress here that the Oh_f -independent behavior does not imply that dissipation is negligible. Indeed, the viscous dissipation in the film

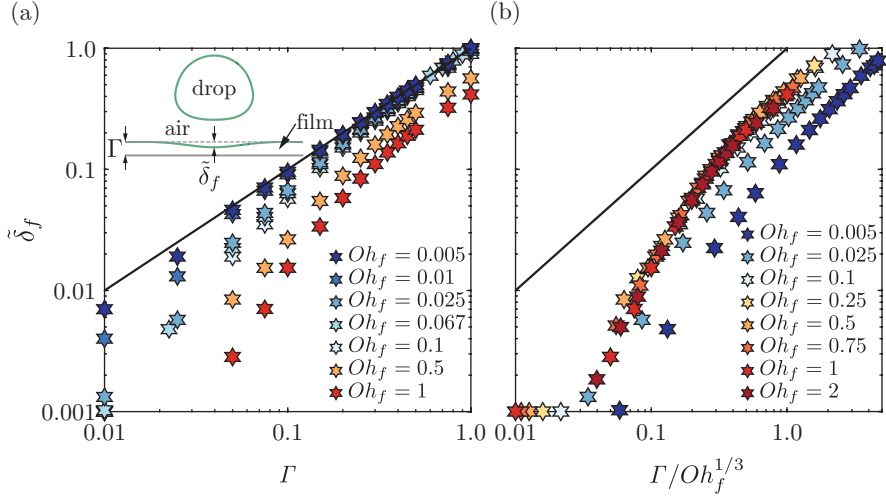


FIGURE 8. Dimensionless film deflection $\tilde{\delta}_f = \delta_f/R$ measured from the initial film free-surface (see the inset in panel a) as a function of (a) the film thickness Γ and (b) the film mobility $\Gamma/Oh_f^{1/3}$ in the direct numerical simulations. The solid black lines represent $\delta_f/R = \Gamma$ and $\delta_f/R = \Gamma/Oh_f^{1/3}$ in panels (a) and (b), respectively. For all cases in this figure, $Oh_d = 0.034$ and $Wed = 4$.

496 accounts for approximately 40% and 85% of the total energy transferred to the film
 497 for $Oh_f = 0.01$ and 0.1, respectively. This difference in the film energy distribution
 498 hints at the failure of our assumptions to neglect the film's inertia and surface tension.
 499 The minimal model is relevant only when the energy transferred to the liquid film is
 500 predominantly lost to viscous dissipation.

501 Guided by the energy budget analysis in the above two extreme cases, we now evidence
 502 the minimal model break down as the film mobility, $\Gamma/Oh_f^{1/3}$, fails to describe the film
 503 deflection δ_f . In figure 8, we report the normalized maximum film deflection $\tilde{\delta}_f = \delta_f/R$
 504 as a function of Γ (figure 8a) for Oh_f in the range 0.01 – 2 while keeping Oh_d constant.
 505 For $Oh_f > 0.1$, the deflection decreases with increasing Oh_f , and the data collapses once
 506 the horizontal axis is rescaled by $Oh_f^{-1/3}$ (figure 8b), confirming the relevance of the film
 507 mobility. However, for lower film Ohnesorge numbers, $\tilde{\delta}_f$ scales with Γ independent of
 508 Oh_f , illustrating the limits of our hypotheses. Here, one might be tempted to empirically
 509 replace the effective control parameter in our model $\propto Oh_f \Gamma^{-3}$ with $\propto \Gamma$, in light of
 510 the $\tilde{\delta}_f$ collapse with $\sim \Gamma$ in the low Oh_f regime. However, such a replacement still fails
 511 to appropriately account for the kinetic and surface energies of the film. Indeed, low
 512 Oh_f films are associated to surface waves, and the maximum deflection δ_f might not be
 513 the correct length scale to mimic their behavior in a simplified model. As future work,
 514 it would be interesting to couple a linearized quasi-potential fluid model (Lee & Kim
 515 2008; Galeano-Rios *et al.* 2017, 2021) for the liquid pool/film with a spring-mass-damper
 516 system for the liquid drop to further investigate this regime.

517 7. Conclusions and Outlook

518 In this work, we perform experiments and direct numerical simulations of the rebound
 519 of an oil drop impacting on a deformable oil film. We elucidate the role of the drop and

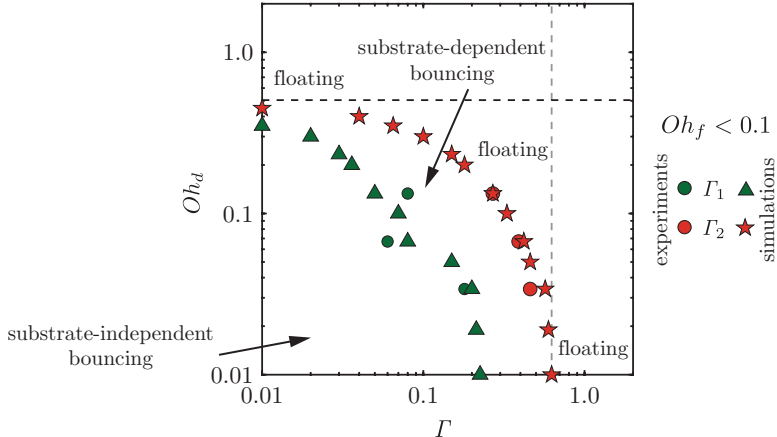


FIGURE 9. Regime map in terms of the drop Ohnesorge number Oh_d and dimensionless film thickness Γ for $Oh_f < 0.1$, showing the transitions between the different regimes identified in this work. Γ_1 (green symbols) marks the transition from substrate-independent bouncing to substrate-dependent bouncing, whereas Γ_2 (red symbols) marks the transition from bouncing to non-bouncing (floating). The black dotted line represents the substrate-independent asymptote for the bouncing to non-bouncing (floating) transition (equation (4.7)), and the gray dotted line, depicting the inviscid drop asymptote for the bouncing to non-bouncing (floating) transition, is drawn as a guide to the eye.

520 film properties: the Ohnesorge numbers of the drop Oh_d and the film Oh_f and the film
 521 thickness Γ on the impact process.

522 For films with a low Ohnesorge number (*i.e.*, $Oh_f < 0.1$), figure 9 summarizes the
 523 different regimes identified in this work. For small film thicknesses, we recover the
 524 substrate-independent limit where bouncing is inhibited by the high viscous dissipation
 525 in the drop ($Oh_{d,c} \sim \mathcal{O}(1)$, Jha *et al.* 2020). Increasing the film thickness reduces the
 526 drop Ohnesorge number marking the bouncing to non-bouncing (floating) transition
 527 as additional energy is transferred to the film, and similarly influences the substrate-
 528 independent to substrate-dependent transition. In the inviscid drop limit, bouncing stops
 529 once a critical film thickness ($\Gamma_2 \sim \mathcal{O}(1)$) is reached, independent of Oh_f . Here, the
 530 invariance of the energy transfer from the drop to the film with Oh_f remains to be
 531 explained and deserves further study.

532 For high Ohnesorge number films (*i.e.*, $Oh_f > 0.1$), figure 10 summarizes the different
 533 regimes identified in this work. Similar to the low Oh_f case, increasing Oh_d and Γ inhibits
 534 bouncing. In contrast with the previous case, in the inviscid drop limit, the bouncing to
 535 non-bouncing (floating) transition occurs at critical film thicknesses that depend on the
 536 Ohnesorge number of the film ($\Gamma_2 \sim Oh_f^{1/3}$). We propose a minimal phenomenological
 537 model describing the key aspects of this process. The background colors in figures 10(a)
 538 and 10(b) illustrate the predicted values of the restitution coefficient ε (equation (4.13))
 539 normalized with its substrate-independent ($\varepsilon^* = \varepsilon(\Gamma/Oh_f^{1/3} \rightarrow 0)$, equation (B 2)),
 540 and inviscid drop and substrate-independent ($\varepsilon_0 = \varepsilon^*(Oh_d \rightarrow 0)$) values, respectively.
 541 The model accurately predicts the substrate-independent and inviscid drop asymptotes
 542 corresponding to the bouncing to non-bouncing (floating) transition, *i.e.* Γ_2 . In the
 543 latter limit, the model also captures the substrate-independent to substrate-dependent
 544 transition (*i.e.*, Γ_1). Away from these asymptotes, the minimal model fails to predict Γ_1
 545 and Γ_2 . We attribute this shortcoming to the simplified representation of the drop-film
 546 interactions in the model. Nonetheless, notice that the predicted values of the restitu-

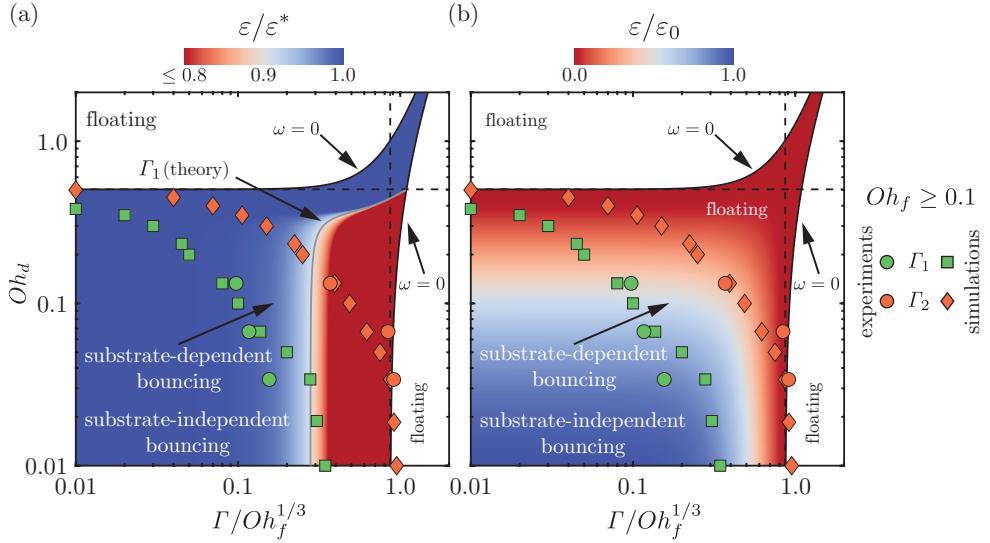


FIGURE 10. Regime map in terms of the drop Ohnesorge number Oh_d and film mobility $\Gamma/Oh_f^{1/3}$ for $Oh_f \geq 0.1$ showing the transitions between the different regimes identified in this work. Γ_1 (green symbols) marks the transition from substrate-independent to substrate-dependent bouncing, whereas Γ_2 (orange symbols) marks the transition from bouncing to non-bouncing (floating). The background contour illustrates the theoretical values of the coefficient of restitution ε (equation (4.13)) normalized with its (a) substrate-independent limit $\varepsilon^* = \varepsilon(\Gamma/Oh_f^{1/3} \rightarrow 0)$, equation (B 2) and (b) inviscid drop and substrate-independent limit $\varepsilon_0 = \varepsilon^*(Oh_d \rightarrow 0)$. The black solid lines shows the predicted bouncing to non-bouncing (floating) transition using the phenomenological model (equations (4.5)-(4.6)), and the black dashed lines show the two asymptotes (equations (4.7)-(4.8)) of bouncing to non-bouncing (floating) regimes. Lastly, in panel (a), the gray solid line shows the prediction for Γ_1 .

tion coefficient are very close to zero beyond the bouncing to non-bouncing (floating) transition observed in the simulations. We hypothesize that the model breakdown might be caused by the neglect of gravity which is known to inhibit bouncing (Biance *et al.* 2006) and may prevent the take off of drops with small upward velocities. We refer the reader to Sanjay *et al.* (2022a) for a detailed study of the role of gravity in inhibiting the bouncing of viscous drops.

Finally, we stress that this study does not present an exhaustive exploration of all bouncing regimes. For example, Lee & Kim (2008); Galeano-Rios *et al.* (2021) have shown that spherical hydrophobic solid spheres can bounce off deep low viscosity pools. Consequently, we hypothesize that the bouncing regime could resurrect at high Oh_d , Γ , and low Oh_f , evidencing non-monotonic energy transfer. It will be interesting to probe such a regime in future work.

Supplementary data. Supplementary material and movies are available at xxxx

Acknowledgements. We acknowledge Esra Van't Westende for carrying out initial experiments. We would like to thank Daniel Harris and Andrea Prosperetti for illuminating discussions. This work was carried out on the national e-infrastructure of SURFsara, a subsidiary of SURF cooperation, the collaborative ICT organization for Dutch education and research.

568 **Funding.** We acknowledge the funding by the ERC Advanced Grant No. 740479-DDD,
 569 European Union's Horizon 2020 research and innovation programme under the Marie
 570 Skłodowska-Curie grant agreement No 722497 and by the Max Planck Center Twente
 571 for Complex Fluid Dynamics.

572
 573 **Declaration of Interests.** The authors report no conflict of interest.
 574

575 **Author ORCID.**

576 V. Sanjay <https://orcid.org/0000-0002-4293-6099>;
 577 S. Lakshman <https://orcid.org/0000-0002-0563-7022>;
 578 P. Chantelot <https://orcid.org/0000-0003-1342-2539>;
 579 J. H. Snoeijer <https://orcid.org/0000-0001-6842-3024>;
 580 D. Lohse <https://orcid.org/0000-0003-4138-2255>.
 581

582 **Appendix A. Air layer rupture**

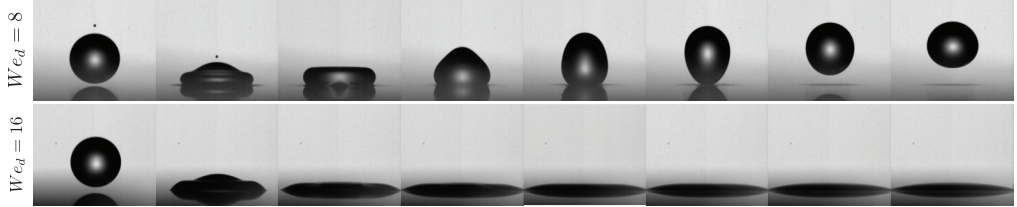
583 We investigate drop bouncing off viscous liquid films that mimic atomically smooth
 584 substrates. The occurrence of such rebounds is tied to the existence of a stable air layer,
 585 enabling drop levitation. It is thus important to determine the conditions leading to air
 586 film rupture in terms of our control parameters. Figure 11(a) illustrates the air layer break
 587 up at large Weber numbers. The air film fails during drop spreading as the intervening
 588 air layer drains below a critical thickness on the order of 10 – 100 nm, characteristic
 589 of the range of van der Waals forces (Charles & Mason 1960; Chubynsky *et al.* 2020;
 590 Zhang *et al.* 2021b). Figure 11(b) evidences the influence of the drop Ohnesorge number
 591 Oh_d on the coalescence transition. At low Oh_d , the convergence of capillary waves at
 592 the drop apex, during the retraction phase, can create an upward Worthington jet and
 593 an associated downward jet due to momentum conservation (Bartolo *et al.* 2006; Lee
 594 *et al.* 2020; Zhang *et al.* 2022). This downward jet can puncture the air film and lead to
 595 coalescence during the drop retraction. Lastly, the air layer can also break due to surface
 596 waves on low Oh_f films (see figure 11c).

597 In summary, figure 11 shows that the critical Weber number beyond which the air layer
 598 between the drop and the film ruptures is sensitive to the Ohnesorge numbers of both the
 599 drop and the film (Tang *et al.* 2016, 2018), and that the bouncing to coalescence transition
 600 can arrest the superamphiphobic-type rebounds discussed in this work. For completeness,
 601 we also mention that a second coalescence transition occurs in our experiments, at times
 602 at least one order of magnitude larger than that associated to drop rebound, when the
 603 air film trapped below a floating drop drains (Lo *et al.* 2017; Duchemin & Josserand
 604 2020). The analysis of both these transitions is beyond the scope of the present study
 605 and we refer the reader to Lohse & Villermaux (2020); Chubynsky *et al.* (2020) for further
 606 discussion and review on this topic.

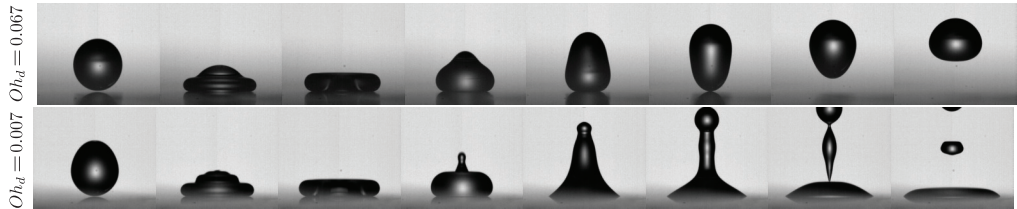
607 **Appendix B. Substrate independent bouncing**

608 As the film thickness decreases or the film viscosity increases, the impact process
 609 becomes independent of the film properties. In this limit, $\Gamma/Oh_f^{1/3} \rightarrow 0$, the phenomeno-
 610 logical model predictions for the contact time and restitution coefficient, equations (4.12)
 611 and (4.13), become

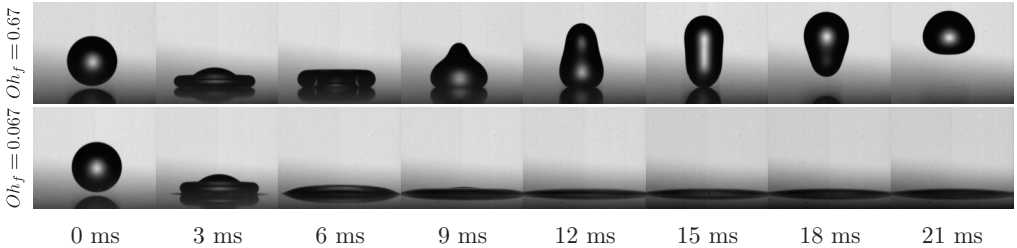
(a) impact-induced rupture ($Oh_d = 0.133, Oh_f = 0.067$)



(b) drop distortion-induced rupture ($We_d = 6, Oh_f = 0.67$)



(c) film distortion-induced rupture ($We_d = 10, Oh_d = 0.067$)



0 ms 3 ms 6 ms 9 ms 12 ms 15 ms 18 ms 21 ms

FIGURE 11. Rupture of the air layer and subsequent coalescence of impacting drops with the liquid coating. Rupture can occur due to: (a) impact as We_d increases, (b) downward jetting as Oh_d decreases, and (c) film distortions due to surface waves as Oh_f decreases. For panels (a) and (c), $\Gamma = 0.03$, and for panel (b) $\Gamma = 0.01$ (dry-substrate limit).

$$t_c^*(Oh_d) = t_c(Oh_d, \Gamma/Oh_f^{1/3} \rightarrow 0) = \tau_\gamma \left(\frac{2\pi}{\sqrt{4c_k - c_d^2 Oh_d^2}} \right), \quad (\text{B } 1)$$

$$\varepsilon^*(Oh_d, We_d) = \varepsilon(Oh_d, We_d, \Gamma/Oh_f^{1/3} \rightarrow 0) = \varepsilon_0(We_d) \exp \left(\frac{-\pi c_d Oh_d}{\sqrt{4c_k - c_d^2 Oh_d^2}} \right), \quad (\text{B } 2)$$

612

613 which are identical to the predictions obtained by [Jha et al. \(2020\)](#) for the impact of
614 viscous drops on a superhydrophobic surface.

615 Reducing equation (B 1) to the case of low viscosity drops ($Oh_d \rightarrow 0$), we get $t_0/\tau_\gamma =$
616 $\pi/\sqrt{c_k}$, as expected from the water-spring analogy ([Richard et al. 2002; Okumura et al.](#)
617 [2003](#)). We thus determine the prefactor c_k by fitting the inviscid limit of our data,
618 $t_0 = 2.2\tau_\gamma$ (figure 12a), yielding $c_k = (\pi\tau_\gamma/t_0)^2 \approx 2$.

619 Furthermore, applying a least square fit to our experimental and numerical data for the
620 coefficient of restitution, which decays exponentially with increasing Oh_d (figure 12b),
621 allows us to fix $c_d = 5.6 \pm 0.1$. Lastly, the model predicts the existence of a critical
622 Ohnesorge number $Oh_{d,c} = 2\sqrt{c_k}/c_d \approx 0.5$ above which the drops do not bounce.

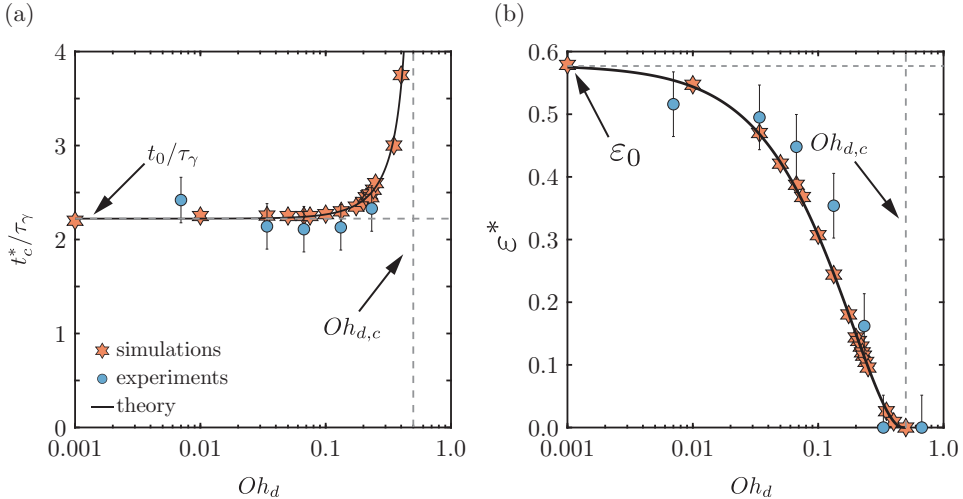


FIGURE 12. Substrate independent bouncing: variation of (a) the contact time t_c^* normalized with the inertia-capillary timescale τ_γ , and (b) the coefficient of restitution ϵ^* with the drop Ohnesorge number Oh_d . The solid black lines represent equations (B 1)-(B 2). These predictions are consistent with those of Jha *et al.* (2020), and set the prefactors c_k and c_d to 2.0 ± 0.1 and 5.6 ± 0.1 , respectively. Here, $We_d = 4$ and $Bo = 0.5$.

623 This asymptote is in quantitative agreement with our data (see the dashed gray lines in
624 figure 12).

625 Finally, we compare the above value of c_d to that obtained by Jha *et al.* (2020). To
626 do so, we note that Jha *et al.* (2020) further reduced equation (B 2) to $\epsilon^*(We_d, Oh_d) \approx$
627 $\epsilon_0(We_d) \exp(-\alpha Oh_d)$, where $\alpha = 2.5 \pm 0.5$ fits their experimental data, independent
628 of the impact Weber number. The equivalent fitting parameter in our case is $\alpha = (\pi/2)c_d/\sqrt{c_k} \approx 6$. This discrepancy can be attributed to the different values of the
629 critical Ohnesorge number $Oh_{d,c}$ which could stem from the Bond number variation
630 between the two cases: $(Oh_{d,c}, Bo) \approx (0.8, 0.2)$, in Jha *et al.* (2020), and $(0.5, 0.5)$ in this
631 work. Exploring the influence of Bo is beyond the scope of this work and we refer the
632 reader to Sanjay *et al.* (2022a) for detailed discussions.
633

634 Appendix C. Influence of the impact Weber number

635 Figure 13 describes the influence of the Weber number We_d on the drop impact process
636 for a representative case with $Oh_d = 0.034$ and $Oh_f = 0.67$. Both the contact time
637 (figure 13a) and the coefficient of restitution (figure 13b) are fairly independent of the
638 Weber number for $We_d \geq 4$. Furthermore, normalizing ϵ with its We_d -dependent value
639 in the dry substrate limit $\epsilon^*(Oh_d, We_d)$, at fixed Oh_d ($= 0.034$ in figure 13), we observe
640 a collapse for $We_d = 2 - 8$, similar to that obtained by Jha *et al.* (2020). Readers
641 are referred to Sanjay *et al.* (2022a) for detailed discussions on the mechanisms of the
642 influence of the Weber number on the coefficient of restitution.

643 Appendix D. Measuring the film thickness

644 Silicone oil films with thicknesses $h_f < 30 \mu\text{m}$, are prepared using spin coating and
645 measured using reflectometry (Reizman 1965). Thicker films ($h_f > 30 \mu\text{m}$) are prepared
646 by depositing a controlled volume of silicone oil on a glass slide. The film thickness is

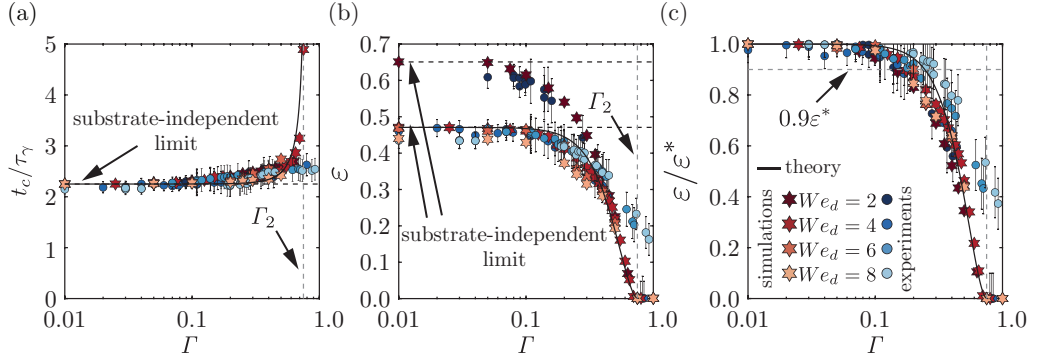


FIGURE 13. Influence of the impact Weber number on the rebound: variation of (a) the contact time t_c normalized with the inertia-capillary time scale τ_γ , (b) the restitution coefficient, and (c) the restitution coefficient normalized with its dry substrate value as a function of the dimensionless film thickness Γ . Here, $(Oh_d, Oh_f) = (0.034, 0.67)$. In each panel, solid black lines represent the model prediction for $(c_k, c_d, c_f) = (2, 5.6, 0.46)$ and the vertical dashed gray line indicate Γ_2 , above which drops do not bounce. In panels (a) and (b), black dashed lines show the W_{ed} -dependent values in the dry substrate limit at fixed Oh_d , i.e., $\varepsilon^*(Oh_d = 0.034, W_{ed})$. Lastly, in panel (c), the horizontal dashed gray line denotes the $0.9\varepsilon^*$ criterion used to determine the substrate-independent to substrate-dependent transition for bouncing drops.

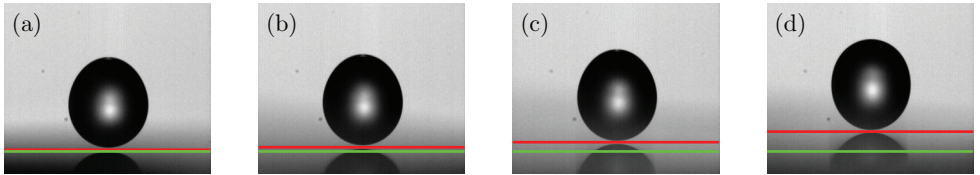


FIGURE 14. Experimental side view snapshots at the instant of impact, $t = 0$. Each snapshot shows the wall location denoted by a green horizontal line and the free-film interface denoted by a red horizontal line. The film thickness is estimated from the vertical difference between the two lines which results in dimensionless film thickness of $\Gamma = h_f/R = 0.05$ (a), 0.11 (b), 0.23 (c), and 0.48 (d).

647 then measured using side view imaging by locating the vertical position of the glass
648 slide wall (green line in figure 14) and of the film free surface (red line in figure 14). The
649 uncertainty in the film thickness measurement using this method is about $\pm 30 \mu\text{m}$, which
650 corresponds to an uncertainty of about 3 pixels.

651 Appendix E. Measuring the restitution coefficient

652 In this appendix, we describe the procedure used to determine the restitution coefficient.
653 In experiments, we measure the drop's maximum center of mass height relative
654 to the undisturbed film surface to get the restitution coefficient as $\varepsilon = \sqrt{2g(H - R)}/V$,
655 where V is the impact velocity. In simulations, we measure the coefficient of restitution
656 as the ratio of the take-off velocity $v_{cm}(t_c)$ to the impact velocity V ,

$$\varepsilon = \frac{v_{cm}(t_c)}{V} \quad (\text{E1})$$

657 where t_c denotes the contact time. The latter definition requires to precisely evaluate the
658 contact time t_c . This is difficult as a thin film of air is always present between the drop
659 and the film surface, we assume ideal non-coalescence between the drop and the film. In

660 simulations, we automatise the detection of the end of apparent contact by taking t_c as
 661 the instant when the normal reaction force $F(t)$ between the film and the drop is zero
 662 (for details on the force calculation, see [Zhang et al. 2022](#)). If the center of mass velocity
 663 $v_{cm}(t_c)$ is not in the upward direction (*i.e.* it is zero or negative), we categorize the case
 664 as non-bouncing.

665 Appendix F. Code availability

666 The codes used in the present article are permanently available at [Sanjay \(2022\)](#).

REFERENCES

- 667 ADDA-BEDIA, M., KUMAR, S., LECHEAULT, F., MOULINET, S., SCHILLACI, M. & VELLA, D.
 668 2016 Inverse Leidenfrost effect: Levitating drops on liquid nitrogen. *Langmuir* **32** (17),
 669 4179–4188.
- 670 BARTOLO, D., JOSSERAND, C. & BONN, D. 2006 Singular jets and bubbles in drop impact. *Phys. Rev. Lett.* **96** (12), 124501.
- 671 BIANCE, A. L., CHEVY, F., CLANET, C., LAGUBEAU, G. & QUÉRÉ, D. 2006 On the elasticity
 672 of an inertial liquid shock. *J. Fluid Mech.* **554**, 47–66.
- 673 BRACKBILL, J. U., KOTHE, D. B. & ZEMACH, C. 1992 A continuum method for modeling
 674 surface tension. *J. Comput. Phys.* **100** (2), 335–354.
- 675 CHANDRA, S. & AVEDISIAN, C. T. 1991 On the collision of a droplet with a solid surface. *Proc. R. Soc. A* **432** (1884), 13–41.
- 676 CHANTELOT, P., COUX, M., CLANET, C. & QUÉRÉ, D. 2018 Drop trampoline. *Europhys. Lett.*
 677 **124** (2), 24003.
- 678 CHANTELOT, P. & LOHSE, D. 2021 Leidenfrost effect as a directed percolation phase transition. *Phys. Rev. Lett.* **127** (12), 124502.
- 679 CHARLES, G. E. & MASON, S. G. 1960 The coalescence of liquid drops with flat liquid/liquid
 680 interfaces. *J. Colloid Interface Sci.* **15** (3), 236–267.
- 681 CHUBYNISKY, M. V., BELOUSOV, K. I., LOCKERBY, D. A. & SPRITTLES, J. E. 2020 Bouncing
 682 off the walls: The influence of gas-kinetic and van der Waals effects in drop impact. *Phys. Rev. Lett.* **124**, 084501.
- 683 COUDER, Y., FORT, E., GAUTIER, C. H. & BOUDAOU, A. 2005a From bouncing to floating:
 684 Noncoalescence of drops on a fluid bath. *Phys. Rev. Lett.* **94** (17), 177801.
- 685 COUDER, Y., PROTIERE, S., FORT, E. & BOUDAOU, A. 2005b Walking and orbiting droplets. *Nature* **437** (7056), 208–208.
- 686 DAVIS, R. H., SCHONBERG, J. A. & RALLISON, J. M. 1989 The lubrication force between two
 687 viscous drops. *Phys. Fluids A* **1** (1), 77–81.
- 688 DE RUITER, J., LAGRAAUW, R., VAN DEN ENDE, D. & MUGELE, F. 2015 Wettability-
 689 independent bouncing on flat surfaces mediated by thin air films. *Nat. Phys.* **11** (1),
 690 48–53.
- 691 DUCHEMIN, L. & JOSSERAND, C. 2020 Dimple drainage before the coalescence of a droplet
 692 deposited on a smooth substrate. *Proc. Natl. Acad. Sci. U.S.A.* **117** (34), 20416–20422.
- 693 EGGLERS, J., FONTELOS, M. A., JOSSERAND, C. & ZALESKI, S. 2010 Drop dynamics after
 694 impact on a solid wall: theory and simulations. *Phys. Fluids* **22** (6), 062101.
- 695 GALEANO-RIOS, C. A., CIMPEANU, R., BAUMAN, I. A., MACEWEN, A., MILEWSKI, P. A.
 696 & HARRIS, D. M. 2021 Capillary-scale solid rebounds: experiments, modelling and
 697 simulations. *J. Fluid Mech.* **912**.
- 698 GALEANO-RIOS, C. A., MILEWSKI, P. A. & VANDEN-BROECK, J.-M. 2017 Non-wetting impact
 699 of a sphere onto a bath and its application to bouncing droplets. *J. Fluid Mech.* **826**,
 700 97–127.
- 701 GAUTHIER, A., DIDDENS, C., PROVILLE, R., LOHSE, D. & VAN DER MEER, D. 2019 Self-
 702 propulsion of inverse Leidenfrost drops on a cryogenic bath. *Proc. Natl. Acad. Sci.* **116** (4),
 703 1174–1179.
- 704 GERI, M., KESHAVARZ, B., MCKINLEY, G. H. & BUSH, J. W. M. 2017 Thermal delay of drop
 705 coalescence. *J. Fluid Mech.* **833**.

- GILET, T. & BUSH, J. W. 2012 Droplets bouncing on a wet, inclined surface. *Phys. Fluids* **24** (12), 122103.
- GILET, T. & BUSH, J. W. M. 2009 The fluid trampoline: droplets bouncing on a soap film. *J. Fluid Mech.* **625**, 167–203.
- HAO, C., LI, J., LIU, Y., ZHOU, X., LIU, Y., LIU, R., CHE, L., ZHOU, W., SUN, D. & LI, L. 2015 Superhydrophobic-like tunable droplet bouncing on slippery liquid interfaces. *Nat. Commun.* **6** (1), 1–7.
- JAYARATNE, O. W. & MASON, B. J. 1964 The coalescence and bouncing of water drops at an air/water interface. *Proc. R. Soc. London, Ser. A* **280** (1383), 545–565.
- JHA, A., CHANTELOT, P., CLANET, C. & QUÉRÉ, D. 2020 Viscous bouncing. *Soft Matter* **16** (31), 7270–7273.
- JOSSERAND, C., RAY, P. & ZALESKI, S. 2016 Droplet impact on a thin liquid film: anatomy of the splash. *J. Fluid Mech.* **802**, 775–805.
- JOSSERAND, CHRISTOPHE & THORODDSEN, SIGURDUR T 2016 Drop impact on a solid surface. *Annu. Rev. Fluid Mech.* **48**, 365–391.
- KLYUZHIN, I. S., IENNA, F., ROEDER, B., WEXLER, A. & POLLACK, G. H. 2010 Persisting water droplets on water surfaces. *J. Phys. Chem. B* **114** (44), 14020–14027.
- KOLINSKI, J. M., MAHADEVAN, L. & RUBINSTEIN, S. M. 2014 Drops can bounce from perfectly hydrophilic surfaces. *Europhys. Lett.* **108** (2), 24001.
- LAKSHMAN, S., TEWES, W., HARTH, K., SNOEIJER, J. H. & LOHSE, D. 2021 Deformation and relaxation of viscous thin films under bouncing drops. *J. Fluid Mech.* **920**.
- LANDAU, L. D. & LIFSHITZ, E. M. 1987 *Fluid Mechanics – Volume 6: Course of Theoretical Physics*, 2nd edn. Elsevier.
- LEAL, L. G. 2007 *Advanced transport phenomena: fluid mechanics and convective transport processes*, , vol. 7. Cambridge University Press.
- LEE, D.-G. & KIM, H.-Y. 2008 Impact of a superhydrophobic sphere onto water. *Langmuir* **24** (1), 142–145.
- LEE, S.-H., RUMP, M., HARTH, K., KIM, M., LOHSE, D., FEZZAA, K. & JE, J. H. 2020 Downward jetting of a dynamic Leidenfrost drop. *Phys. Rev. Fluids* **5** (7), 074802.
- LEIDENFROST, J. G. 1756 *De aquae communis nonnullis qualitatibus tractatus*. Ovenius.
- LI, E. Q., VAKARELSKI, I. U. & THORODDSEN, S. T. 2015 Probing the nanoscale: the first contact of an impacting drop. *J. Fluid Mech.* **785**, R2.
- LING, Y., FUSTER, D., ZALESKI, S. & TRYGGVASON, G. 2017 Spray formation in a quasiplanar gas-liquid mixing layer at moderate density ratios: a numerical closeup. *Phys. Fluids* **2** (1), 014005.
- LO, H. Y., LIU, Y. & XU, L. 2017 Mechanism of contact between a droplet and an atomically smooth substrate. *Phys. Rev. X* **7** (2), 021036.
- LOHSE, D. 2022 Fundamental fluid dynamics challenges in inkjet printing. *Annu. Rev. Fluid Mech.* **54**, 349–382.
- LOHSE, D. & VILLERMAUX, E. 2020 Double threshold behavior for breakup of liquid sheets. *Proc. Natl. Acad. Sci. USA* **117**, 18912–18914.
- MOLÁČEK, J. & BUSH, J. W. 2012 A quasi-static model of drop impact. *Phys. Fluids* **24** (12), 127103.
- NARU, M. C. 2021 Numerical simulation of a water/oil emulsion in a multiscale/multiphysics context. PhD thesis, EDSorbonne University.
- OKUMURA, K., CHEVY, F., RICHARD, D., QUÉRÉ, D. & CLANET, C. 2003 Water spring: A model for bouncing drops. *Europhys. Lett.* **62** (2), 237.
- PACK, M., HU, H., KIM, D., ZHENG, Z., STONE, H. A. & SUN, Y. 2017 Failure mechanisms of air entrainment in drop impact on lubricated surfaces. *Soft Matter* **13** (12), 2402–2409.
- PAL, S., MIQDAD, A. M., DATTA, S., DAS, A. K. & DAS, P. K. 2017 Control of drop impact and proposal of pseudo-superhydrophobicity using electrostatics. *Ind. Eng. Chem. Res.* **56** (39), 11312–11319.
- PAN, K. L. & LAW, C. K. 2007 Dynamics of droplet–film collision. *J. Fluid Mech.* **587**, 1–22.
- POPINET, S. 2009 An accurate adaptive solver for surface-tension-driven interfacial flows. *J. Comput. Phys.* **228** (16), 5838–5866.
- POPINET, S. 2015 A quadtree-adaptive multigrid solver for the Serre-Green-Naghdi equations. *J. Comput. Phys.* **302** (336–358).

- 768 POPINET, S. & COLLABORATORS 2013–2022a Basilisk C. <http://basilisk.fr> (Last accessed:
769 March 3, 2022).
- 770 POPINET, S. & COLLABORATORS 2013–2022b Basilisk C: surface tension library. [http://
771 basilisk.fr/src/tension.h](http://basilisk.fr/src/tension.h) (Last accessed: March 3, 2022).
- 772 PROSPERETTI, A. 1977 Viscous effects on perturbed spherical flows. *Q. Appl. Math.* **34** (4),
773 339–352.
- 774 PROSPERETTI, A. & TRYGGVASON, G. 2009 *Computational Methods for Multiphase Flow*.
775 Cambridge university press.
- 776 QUÉRÉ, D. 2013 Leidenfrost dynamics. *Annu. Rev. Fluid Mech.* **45**, 197–215.
- 777 RAMÍREZ-SOTO, O., SANJAY, V., LOHSE, D., PHAM, J. T. & VOLLMER, D. 2020 Lifting a
778 sessile oil drop from a superamphiphobic surface with an impacting one. *Sci. Adv.* **6** (34),
779 eaba4330.
- 780 RAYLEIGH, LORD 1879 On the capillary phenomena of jets. *Proc. R. Soc. London* **29** (196–199),
781 71–97.
- 782 REIN, M. 1993 Phenomena of liquid drop impact on solid and liquid surfaces. *Fluid Dyn. Res.*
783 **12** (2), 61.
- 784 REIZMAN, F. 1965 Optical thickness measurement of thin transparent films on silicon. *J. Appl.
785 Phys.* **36** (12), 3804–3807.
- 786 REYNOLDS, O. 1881 On the floating of drops on the surface of water depending only on the
787 purity of the surface. *Proc. Lit. Phil. Soc.* **21** (1), 413–414.
- 788 RICHARD, D., CLANET, C. & QUÉRÉ, D. 2002 Contact time of a bouncing drop. *Nature*
789 **417** (6891), 811–811.
- 790 RODRIGUEZ, F. & MESLER, R. 1985 Some drops don't splash. *J. Colloid Interface Sci.* **106** (2),
791 347–352.
- 792 SANJAY, V. 2022 Code repository: Drop impact on viscous liquid films. [https://github.com/
793 VatsalSy/Drop-impact-on-viscous-liquid-films](https://github.com/VatsalSy/Drop-impact-on-viscous-liquid-films) (Last accessed: April 1, 2022).
- 794 SANJAY, V., CHANTELOT, P. & LOHSE, D. 2022a When does an impacting drop stop bouncing?
795 *arXiv preprint arXiv:2208.05935*.
- 796 SANJAY, V., SEN, U., KANT, P. & LOHSE, D. 2022b Taylor-Culick retractions and the influence
797 of the surroundings. *J. Fluid Mech.* **948**, A14.
- 798 SCHUTZIUS, T. M., JUNG, S., MAITRA, T., GRAEBER, G., KÖHME, M. & POULIKAKOS, D. 2015
799 Spontaneous droplet trampolining on rigid superhydrophobic surfaces. *Nature* **527** (7576),
800 82–85.
- 801 SHARMA, P. K. & DIXIT, H. N. 2021 Regimes of wettability-dependent and wettability-
802 independent bouncing of a drop on a solid surface. *J. Fluid Mech.* **908**.
- 803 SHIROTA, M., VAN LIMBEEK, M. A. J., SUN, C., PROSPERETTI, A. & LOHSE, D. 2016 Dynamic
804 Leidenfrost effect: Relevant time and length scales. *Phys. Rev. Lett.* **116** (6), 064501.
- 805 SINGH, C., DAS, A. K. & DAS, P. K. 2018 Levitation of non-magnetizable droplets inside
806 ferrofluid. *J. Fluid Mech.* **857**, 398–448.
- 807 SMITH, F. R., NICLOUX, C. & BRUTIN, D. 2018 Influence of the impact energy on the pattern
808 of blood drip stains. *Phys. Rev. Fluids* **3** (1), 013601.
- 809 SMITH, F. T., LI, L. & WU, G. X. 2003 Air cushioning with a lubrication/inviscid balance. *J.
810 Fluid Mech.* **482**, 291–318.
- 811 TANG, X., SAHA, A., LAW, C.K. & SUN, C. 2016 Nonmonotonic response of drop impacting
812 on liquid film: mechanism and scaling. *Soft Matter* **12** (20), 4521–4529.
- 813 TANG, X., SAHA, A., LAW, C. K. & SUN, C. 2018 Bouncing-to-merging transition in drop
814 impact on liquid film: Role of liquid viscosity. *Langmuir* **34** (8), 2654–2662.
- 815 TANG, X., SAHA, A., LAW, C. K. & SUN, C. 2019 Bouncing drop on liquid film: Dynamics of
816 interfacial gas layer. *Phys. Fluids* **31** (1), 013304.
- 817 TERWAGNE, D., LUDEWIG, F., VANDEWALLE, N. & DORBOLO, S. 2013 The role of the droplet
818 deformations in the bouncing droplet dynamics. *Phys. Fluids* **25** (12), 122101.
- 819 THORODDSEN, S. T., ETOH, T. G. & TAKEHARA, K. 2003 Air entrapment under an impacting
820 drop. *J. Fluid Mech.* **478**, 125–134.
- 821 THORODDSEN, S. T., ETOH, T. G. & TAKEHARA, K. 2008 High-speed imaging of drops and
822 bubbles. *Annu. Rev. Fluid Mech.* **40**, 257–285.
- 823 TRAN, T., STAAT, H. J. J., PROSPERETTI, A., SUN, C. & LOHSE, D. 2012 Drop impact on
824 superheated surfaces. *Phys. Rev. Lett.* **108** (3), 036101.

- TRYGGVASON, G., SCARDOVELLI, R. & ZALESKI, S. 2011 *Direct numerical simulations of gas-liquid multiphase flows*. Cambridge University Press.
- VAN DER VEEN, R. C., TRAN, T., LOHSE, D. & SUN, C. 2012 Direct measurements of air layer profiles under impacting droplets using high-speed color interferometry. *Phys. Rev. E* **85** (2), 026315.
- WACHTERS, L. H. J. & WESTERLING, N. A. J. 1966 The heat transfer from a hot wall to impinging water drops in the spheroidal state. *Chem. Eng. Sci.* **21** (11), 1047–1056.
- WEISS, D. A. & YARIN, A. L. 1999 Single drop impact onto liquid films: neck distortion, jetting, tiny bubble entrainment, and crown formation. *J. Fluid Mech.* **385**, 229–254.
- WILDEMAN, S., VISSER, C. W., SUN, C. & LOHSE, D. 2016 On the spreading of impacting drops. *J. Fluid Mech.* **805**, 636–655.
- WORTHINGTON, A. M. 1877 On the forms assumed by drops of liquids falling vertically on a horizontal plate. *Proc. R. Soc. London, Ser. A* **25** (171–178), 261–272.
- WORTHINGTON, A. M. 1908 *A study of splashes*. London: Longman, Green and Co.
- WU, Z., HAO, J., LU, J., XU, L., HU, G. & FLORYAN, J. M. 2020 Small droplet bouncing on a deep pool. *Phys. Fluids* **32** (1), 012107.
- YARIN, A. L. 2006 Drop impact dynamics: splashing, spreading, receding, bouncing.... *Annu. Rev. Fluid Mech.* **38**, 159–192.
- YARIN, A. L., ROISMAN, I. V. & TROPEA, C. 2017 *Collision Phenomena in Liquids and Solids*. Cambridge University Press.
- YIANTSIOS, S. G. & DAVIS, R. H. 1990 On the buoyancy-driven motion of a drop towards a rigid surface or a deformable interface. *J. Fluid Mech.* **217**, 547–573.
- YIANTSIOS, S. G. & DAVIS, R. H. 1991 Close approach and deformation of two viscous drops due to gravity and van der Waals forces. *J. Colloid Interface Sci.* **144** (2), 412–433.
- ZHANG, B., SANJAY, V., SHI, S., ZHAO, Y., LV, C. & LOHSE, D. 2022 Impact forces of water drops falling on superhydrophobic surfaces. *Phys. Rev. Lett.* **129** (10), 104501.
- ZHANG, J., NI, M.-J. & MAGNAUDET, J. 2021a Three-dimensional dynamics of a pair of deformable bubbles rising initially in line. part 1. moderately inertial regimes. *J. Fluid Mech.* **920**, A16.
- ZHANG, L., SOORI, T., ROKONI, A., KAMINSKI, A. & SUN, Y. 2021b Thin film instability driven dimple mode of air film failure during drop impact on smooth surfaces. *Phys. Rev. Fluids* **6** (4), 044002.